Single-Pulse Simultaneous Target Detection and Angle Estimation in a Multichannel Phased Array Radar

Augusto Aubry, *Senior Member, IEEE*, Antonio De Maio, *Fellow, IEEE*, Stefano Marano, *Senior Member, IEEE* and Massimo Rosamilia, *Student Member, IEEE*

***Abstract*—This paper is focused on simultaneous target detection and angle estimation with a multichannel phased array radar. Resorting to a linearized expression for the array steering vector around the beam pointing direction, the problem is formulated as a composite binary hypothesis test where the unknowns, under the alternative hypothesis, include the target directional cosines displacements with respect to the array nominal coarse pointing direction. The problem is handled via the Generalized Likelihood Ratio (GLR) criterion (both one-step and two-step) where decision statistics leveraging the Maximum Likelihood Estimates (MLEs) of the parameters are compared with a detection threshold. If crossed, target presence is declared and the MLEs of the aforementioned displacements directly provide target angular position with respect to the pointing direction. From the analytic point of view, ML estimation involves a constrained fractional quadratic optimization problem whose optimal solution can be found via the Dinkelbach's algorithm or approximated through a fast-converging procedure based on a Coordinate Descent (CD) optimization. The performance analysis of the proposed architectures as well as the corresponding discussion is developed in terms of computational complexity, Constant False Alarm Rate (CFAR) behavior, detection performance, and angular estimation accuracy, also in comparison with some counterparts available in the open literature and theoretical benchmark limits.**

I. Introduction

Multichannel phased array radar systems must comply with very stressing operational requirements demanding for surveillance at specific ranges, sometimes with different update rates depending on the different elevation sectors; tracking with variable update rates that can be different from those adopted in the search task; 3-D target data measurements; the capability to manage many tracks simultaneously without decreasing the search performance and the capability to operate in clutter and jamming environments [2]–[5]. Agility in beam steering and adaptive digital beamforming are key ingredients to face the challenge together with advanced signal and data processing algorithms aimed at boosting the radar performance [6], [7]. At the root of all the mentioned processes there is target detection and its localization within a 3-D coordinate system.

Historically, as testified by the many references available in the open literature [8]–[17], target angle estimation (usually performed in the directional cosines domain [8], [10]) is activated after a detection event is triggered. This also motivates why detection and target angle estimation are addressed as two distinct signal processing tasks. First detection of a mainbeam target is performed via an adaptive detector [18]–[27], chosen to balance different performance tradeoffs (matched detection performance, rejection of sidelobe targets, robustness with respect to mismatched targets, computational complexity). Then, if the presence of a target is declared within the antenna mainbeam, a specific angle estimation technique such as Maximum Likelihood (ML) [10], monopulse [17], generalized monopulse [8], Generalized Adaptive Multidimensional Monopulse Algorithm (GAMMA) [13] is initiated to localize the target within the antenna beam.

The approach pursued in this paper relies on the idea of performing jointly target detection and accurate angular estimation, namely the angle coordinates are directly provided with single pulse spatial processing simultaneously with target detection. If the resulting processing is capable of granting a computational complexity compatible with real time constraints, it can be implemented for every search beam of a multifunction phased array radar. Otherwise, it turns out very useful in the target confirmation (verification) process [3] where, after a first detection is triggered by a standard detector, one needs to confirm the target presence (lowering the False Alarm Probability (P_{fa})) and to output angular estimates.

Before continuing with the description of the present approach, it is worth observing that the idea of joint target detection and localization/estimation has been pursued also in other studies available in the open literature possibly referring to different localization domain, such as range [28], [29], parameters of interest, e.g., motion parameters [30], or different system configurations, e.g., Multiple Input Multiple Output (MIMO) radar with widely displaced antennas [31].

For a joint target detection and angle estimation, after a tailored linearization procedure, the target steering vector is represented as the superposition of the pointing direction term plus two contributions that account for the directional cosines offsets with respect the nominal array steering. Based on this representation, target detection in the presence of interference

Augusto Aubry, Antonio De Maio (Corresponding Author) and Massimo Rosamilia are with Università degli Studi di Napoli "Federico II", DIETI, Via Claudio 21, I-80125 Napoli, Italy. E-mail: augusto.aubry@unina.it, ademaio@unina.it, massimo.rosamilia@unina.it.

Stefano Marano is with the Dipartimento di Ingegneria dell'Informazione ed Elettrica e Matematica Applicata, University of Salerno, Fisciano I-84084, Italy. E-mail: marano@unisa.it.

Part of this paper has been presented at the 2020 IEEE Radar Conference (RadarConf20) [1].

This paper has supplementary downloadable material available at http://ieeexplore.ieee.org., provided by the author. The material includes a PDF file providing some additional theoretical derivations/details as well as further numerical results. This material is 343 KB in size.

is cast as a binary composite hypothesis testing problem with a different number of unknowns under the two alternatives. In particular, under the $\mathcal{H}_1$ hypothesis, i.e., target presence, the likelihood function exhibits dependence on the complex target amplitude, the interference covariance matrix, and the two direction cosine displacement parameters (accounting for the unknown target location within the array mainbeam). This formulation paves the way for the development of signal processing architectures which are able to detect the target and, at the same time, to determine its angular estimate. In this respect, the Generalized Likelihood Ratio Test (GLRT) criterion [18], [32] is considered, which under the $\mathcal{H}_1$ hypothesis, after concentration over the unknown interference covariance and target complex amplitude, demands the solution of an optimization problem over the unknown direction offsets. For the special case of 1-D linear array the problem is solved in closed form by simply computing the roots of a second-order equation. For the 2-D planar array, the optimization becomes more challenging and falls within the class of box-constrained fractional quadratic problems. In this regard, two new solution methods are proposed. The former provides the optimal solution and relies on the use of the Dinkelbach's algorithm [33]–[35]. The latter is an iterative fast-converging procedure based on a Coordinate Descent (CD) optimization [36]. However, in this last case, only convergence to a stationary point can be claimed.

At the analysis stage, the new GLRT-based signal processing architectures are compared with classic detectors such as Kelly's GLRT [19], Adaptive Matched Filter (AMF) [20], Subspace Detector (SD) [18], [21], [37] in terms of detection performance. Besides, the mean square error of the angular estimates are compared with the Cramer Rao Lower Bound (CRLB) [10], ML [10], and the adaptive monopulse (devised in [17] and also described in [9]). The results highlight that the bespoke new methodology is a very effective candidate to solve the problem of joint target detection and angular estimation, providing close-to-optimum detection performances and high quality angular estimates in many scenarios of practical relevance for modern phased array radar.

The paper is organized as follows. Section II deals with problem formulation. In Section III, three procedures to solve the constrained optimization problem are developed. Section IV addresses the performance analysis and outlines comparisons for both detection and estimation tasks. Finally, Section V, summarizes conclusions and outlines possible future research avenues.

A. Notation

Boldface is used for vectors $\boldsymbol{a}$ (lower case), and matrices $\boldsymbol{A}$ (upper case). The (k,l)-entry (or l-entry) of a generic matrix $\boldsymbol{A}$ (or vector $\boldsymbol{a}$) is indicated as $\boldsymbol{A}(k,l)$ (or $\boldsymbol{a}(l)$). $\boldsymbol{I}$ and $\boldsymbol{0}$ denote the identity matrix and the matrix with zero entries, respectively (their size is determined from the context). The all-ones column vector of size N is denoted by $\boldsymbol{1}_N$. The transpose, the conjugate, and the conjugate transpose operators are denoted by the symbols $(\cdot)^T$, $(\cdot)^*$, and $(\cdot)^\dagger$, respectively. The Kronecker and Hadamard (i.e., elementwise) products are indicated as $\otimes$ and $\odot$, respectively. $\mathbb{R}^N$, $\mathbb{C}^N$, and $\mathbb{H}^N$ are respectively the sets of N-dimensional vectors of real numbers, of N-dimensional column vectors of complex numbers, and of $N \times N$ Hermitian matrices. The curled inequality symbol $\succeq$ (and its strict form $\succ$) is used to denote generalized matrix inequality: for any $\boldsymbol{A} \in \mathbb{H}^N$, $\boldsymbol{A} \succeq \boldsymbol{0}$ means that $\boldsymbol{A}$ is a positive semi-definite matrix ($\boldsymbol{A} \succ \boldsymbol{0}$ for positive definiteness). The letter j represents the imaginary unit (i.e., $j = \sqrt{-1}$). For any complex number x, $\mathrm{Re}\{x\}$ and $|x|$ indicate the real part and the modulus of x, respectively. Moreover, for any $\boldsymbol{x} \in \mathbb{C}^N$, $\|\boldsymbol{x}\|$ represents the Euclidean norm of $\boldsymbol{x}$. Finally, $E[\cdot]$ denotes statistical expectation and $v \sim U(-\Delta, \Delta)$ indicates a random variable v uniformly distributed over $(-\Delta, \Delta)$, $\Delta > 0$.

II. Problem Formulation

Let us consider a radar system that collects spatial data via a narrow-band planar array (see Fig. 1) composed of NM antennas. After down-conversion, pulse compression, and fast-time sampling, the echo signal induced by a prospective target located at range R, azimuth θ_0, and elevation ϕ_0 with respect to array boresight, is given by

$$a\boldsymbol{p}(u_0, v_0), \tag{1}$$

where a is an unknown complex parameter accounting for target backscattering and channel propagation effects, (u_0, v_0) indicates the target angular location in the space of directional cosines [10], i.e.,

$$u_0 = \sin(\theta_0)\cos(\phi_0), \quad v_0 = \sin(\theta_0)\sin(\phi_0), \tag{2}$$

and $\boldsymbol{p}(u_0, v_0)$ denotes the spatial steering vector $\boldsymbol{p}(u, v)$ evaluated at (u_0, v_0). For a Uniform Rectangular Array (URA)

$$\boldsymbol{p}(u, v) = \boldsymbol{p}_u(u) \otimes \boldsymbol{p}_v(v), \tag{3}$$

with

$$\boldsymbol{p}_u(u) = [e^{j\frac{2\pi}{\lambda_0}x_0 u}, e^{j\frac{2\pi}{\lambda_0}x_1 u}, \ldots, e^{j\frac{2\pi}{\lambda_0}x_{N-1} u}]^T \in \mathbb{C}^N, \tag{4}$$

$$\boldsymbol{p}_v(v) = [e^{j\frac{2\pi}{\lambda_0}y_0 v}, e^{j\frac{2\pi}{\lambda_0}y_1 v}, \ldots, e^{j\frac{2\pi}{\lambda_0}y_{M-1} v}]^T \in \mathbb{C}^M, \tag{5}$$

where $(x_i, y_h), \quad i = 0, \ldots, N-1, \ h = 0, \ldots, M-1$, are the positions[1] of the array elements and λ_0 is the radar operating wavelength.

Assuming the potential useful echo signal buried in Gaussian interference with unknown spectral characteristics and supposing the availability of $K \geq N$ homogeneous secondary data (i.e., data vectors, free of useful target returns, exhibiting the same spectral property as that from the cell under test),

[1]For a URA, denoting by d_x and d_y the interelement spacing (usually given by $\lambda_0/2$) along the x and y axes, respectively, if the reference system center is located in the bottom-left corner

$$x_i = d_x\, i, \ \ i = 0, 1, \ldots, N-1, \ \ y_h = d_y\, h, \ h = 0, 1, \ldots, M-1.$$

If instead the reference system center coincides with the array center, then

$$x_i = d_x \ \left(i - \left(\tfrac{N-1}{2}\right)\right), \ i = 0, 1, \ldots, N-1,$$
$$y_h = d_y \ \left(h - \left(\tfrac{M-1}{2}\right)\right), \ h = 0, 1, \ldots, M-1.$$

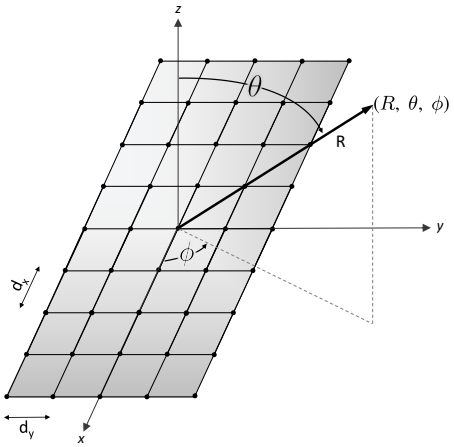

Fig. 1. Two dimensional symmetric planar array geometry with equi-spaced antennas in the x and y directions. (R, θ, ϕ) are the polar coordinates of target.

the problem of detecting a target located at (θ_0, ϕ_0), i.e., at (u_0, v_0) in $u-v$ space, can be formulated as the following composite binary hypothesis testing problem

$$\begin{cases} \mathcal{H}_0 : \begin{cases} \boldsymbol{r} = \boldsymbol{n} \\ \boldsymbol{r}_k = \boldsymbol{n}_k \quad k = 1, \ldots, K \end{cases} \\ \mathcal{H}_1 : \begin{cases} \boldsymbol{r} = a\boldsymbol{p}(u_0, v_0) + \boldsymbol{n} \\ \boldsymbol{r}_k = \boldsymbol{n}_k \quad k = 1, \ldots, K \end{cases} \end{cases}, \tag{6}$$

where the interference plus noise components $\boldsymbol{n}$ and $\boldsymbol{n}_k$, $k = 1, \ldots, K$, are modeled as statistically independent, complex, zero-mean, circularly symmetric Gaussian random vectors with unknown positive definite covariance matrix

$$\boldsymbol{M} = E[\boldsymbol{n}\boldsymbol{n}^\dagger] = E[\boldsymbol{n}_k\boldsymbol{n}_k^\dagger], \quad k = 1, \ldots, K. \tag{7}$$

Two important remarks are now necessary.

1) The presented framework is developed using a URA, but it can be easily generalized to deal with different types of array. Besides, for the special case of a linear array, i.e., $M = 1$, the steering vector (3) degenerates into (4).
2) The interference scenario with the assumptions in (7) defines the so called "homogeneous environment", well established and accepted in radar detection-estimation literature being theoretically justified and representative of many practical operative contexts [19], [20], [38], [39] and also explained in many technical books [6], [9], [18].

A. Pointing Errors

An array steering direction is not usually aligned with the target Direction of Arrival (DOA), especially when the radar is in search mode. In order to account for this mismatch, a specific model of the array steering vector is now developed, leveraging a linearization of the array manifold around the transmit look-direction $(\bar{u}, \bar{v})$. Specifically, denoting by $(\Delta u, \Delta v)$ the directional cosine offset, i.e., $\Delta u = u_0 - \bar{u}$, $\Delta v = v_0 - \bar{v}$, the target steering vector is approximated as

$$\boldsymbol{p}_a(\Delta u, \Delta v) = \boldsymbol{p}(\bar{u}, \bar{v}) + \frac{\partial \boldsymbol{p}(\bar{u}, \bar{v})}{\partial u}\Delta u + \frac{\partial \boldsymbol{p}(\bar{u}, \bar{v})}{\partial v}\Delta v, \tag{8}$$

where the explicit dependence of the approximated steering vector on the pointing direction is omitted to avoid unnecessary notational complications. Note that

$$\begin{aligned} &\frac{\partial \boldsymbol{p}(\bar{u}, \bar{v})}{\partial u} = \left.\frac{\partial \boldsymbol{p}(u, v)}{\partial u}\right|_{\substack{u=\bar{u} \\ v=\bar{v}}} = \\ &j\frac{2\pi}{\lambda_0}\left(\boldsymbol{p}_u(\bar{u}) \odot [x_0, x_1, \ldots, x_{N-1}]^T\right) \otimes \boldsymbol{p}_v(\bar{v}) \end{aligned} \tag{9}$$

and

$$\begin{aligned} &\frac{\partial \boldsymbol{p}(\bar{u}, \bar{v})}{\partial v} = \left.\frac{\partial \boldsymbol{p}(u, v)}{\partial v}\right|_{\substack{u=\bar{u} \\ v=\bar{v}}} = \\ &j\frac{2\pi}{\lambda_0}\boldsymbol{p}_u(\bar{u}) \otimes \left(\boldsymbol{p}_v(\bar{v}) \odot [y_0, y_1, \ldots, y_{M-1}]^T\right) \end{aligned} \tag{10}$$

represent the partial derivatives with respect to u and v.

To assess the accuracy of the approximation in (8), Fig. 2 reports the magnitude of the normalized correlation (mismatched angle cosine) between the actual steering vector and the approximated one, i.e.,

$$\frac{|\boldsymbol{p}_a(\Delta u, \Delta v)^\dagger \boldsymbol{p}(\bar{u} + \Delta u, \bar{v} + \Delta v)|}{\|\boldsymbol{p}_a(\Delta u, \Delta v)\| \, \|\boldsymbol{p}(\bar{u} + \Delta u, \bar{v} + \Delta v)\|}, \tag{11}$$

versus the directional cosines offsets. Specifically, assuming symmetric array configurations, in Fig. 2(a) the 1-D case is analyzed, with $N = 9$ and $\bar{u} = 0$, whereas Fig. 2(b) refers to the 2-D scenario with $M = 5, N = 5, \bar{u} = \bar{v} = 0$. The results clearly highlight the ability of $\boldsymbol{p}_a(\Delta u, \Delta v)$ to describe accurately the actual steering vector as long as the target DOA lies within the 3 dB beamwidth. Indeed, normalized correlation values higher than 0.83 are achieved[2] if $|\Delta u| \leq 0.891/N$ and $|\Delta v| \leq 0.891/M$ where $0.891/N$ and $0.891/M$ represent the 3 dB single-side beamwidth of a planar array pointing at the boresight direction.

Hereafter, to simplify notation, the nominal steering vector $\boldsymbol{p}(\bar{u}, \bar{v})$ is indicated as $\boldsymbol{p}$ whereas the steering derivatives (at the pointing directions) $\partial \boldsymbol{p}(\bar{u}, \bar{v})/\partial u$ and $\partial \boldsymbol{p}(\bar{u}, \bar{v})/\partial v$ are denoted by $\dot{\boldsymbol{p}}_u$ and $\dot{\boldsymbol{p}}_v$, respectively. As a result, equation (8) can be re-written as

$$\boldsymbol{p}_a(\Delta u, \Delta v) = \boldsymbol{p} + \boldsymbol{H}\boldsymbol{\Delta\theta}, \tag{12}$$

with $\boldsymbol{H} = [\dot{\boldsymbol{p}}_u, \dot{\boldsymbol{p}}_v]$ the Jacobian matrix, and $\boldsymbol{\Delta\theta} = [\Delta u, \Delta v]^T \in \mathbb{R}^2$. Note that, for the special case of a linear array, the steering model boils down to

$$\boldsymbol{p}_a(\Delta u) = \boldsymbol{p}_u(\bar{u}) + \frac{\partial \boldsymbol{p}(\bar{u})}{\partial u}\Delta u = \boldsymbol{p} + \dot{\boldsymbol{p}}_u\Delta u. \tag{13}$$

Now, leveraging the useful signal model (12), the target detection problem in the presence of pointing errors can be cast as

$$\begin{cases} \mathcal{H}_0 : \begin{cases} \boldsymbol{r} = \boldsymbol{n} \\ \boldsymbol{r}_k = \boldsymbol{n}_k \quad k = 1, \ldots, K \end{cases} \\ \mathcal{H}_1 : \begin{cases} \boldsymbol{r} = a\boldsymbol{p}_a(\Delta u, \Delta v) + \boldsymbol{n} \\ \boldsymbol{r}_k = \boldsymbol{n}_k \quad k = 1, \ldots, K \end{cases} \end{cases}, \tag{14}$$

where $\boldsymbol{p}_a(\Delta u, \Delta v)$ represents the approximated steering vec-

[2]Normalized correlation values larger than or equal to 0.95 are achieved in 1-D case provided that $|\Delta u| \leq 0.891/N$.

tor and the entries of $(\Delta u, \Delta v)$ indicate the unknown target direction cosines, with $|\Delta u| \leq \alpha,\ |\Delta v| \leq \beta$. The choice of the constraint levels α and β must reflect a compromise between DOA uncertainty and quality of the linear approximation. A reasonable choice is the 3 dB single-side beamwidth[3].

Before concluding this section, it is worth stressing the major differences between our model and the classic subspace framework [21]. Both characterize the useful signal contribution as the superposition of three components, i.e., $\boldsymbol{s}_t = \alpha_1 \boldsymbol{p} + \alpha_2 \boldsymbol{p}_2 + \alpha_3 \boldsymbol{p}_3$, with $\alpha_i \in \mathbb{C}, i = 1, 2, 3$. However, unlike the subspace model, the useful-signal uncertainty set in (14) is non-convex and the weights are structured so that their values are representative directly of the target DOA displacements in $u - v$ space. Specifically, α_2/α_1 and α_3/α_1 provide the DOA offset along the u and v axis, respectively. Furthermore, capitalizing the a-priori information on the sensing system, namely the transmit beamwidth size, the feasible values of the unknowns DOA displacements can be appropriately constrained, laying the ground for an improved angular estimation.

III. System Design: Joint Detection and Angle Estimation

The optimum solution to the hypotheses testing problem (14) (in the Neyman-Pearson sense) is the likelihood ratio test (LRT). However, its practical implementation is precluded as the knowledge of the parameters Δu, Δv, a and $\boldsymbol{M}$ is required. In detection theory jargon this means that a Uniformly Most Powerful (UMP) test does not exist. Thus, to come up with a practically implementable receiver, the GLR criterion is exploited, where the unknown parameters are replaced by their ML estimates under each hypothesis. Specifically, the following constrained GLRT decision rule is proposed

$$\frac{\max\limits_{\substack{\boldsymbol{M}, a, \\ |\Delta u| \leq \alpha\ |\Delta v| \leq \beta}} f_{\mathcal{H}_1}(\boldsymbol{r}, \boldsymbol{r}_1, \ldots, \boldsymbol{r}_k | \boldsymbol{M}, a, \boldsymbol{\Delta\theta})}{\max\limits_{\boldsymbol{M}} f_{\mathcal{H}_0}(\boldsymbol{r}, \boldsymbol{r}_1, \ldots, \boldsymbol{r}_k | \boldsymbol{M})} \underset{\mathcal{H}_0}{\overset{\mathcal{H}_1}{\gtrless}} T, \tag{15}$$

where $f_{\mathcal{H}_1}(\cdot)$ and $f_{\mathcal{H}_0}(\cdot)$ represent the probability density functions of the observations under the two hypotheses, and T is the detection threshold[4] set to ensure a desired P_{fa}. Besides, the AMF version of (15) (also known as two-step GLRT because it can be obtained computing the GLRT from the primary data vector (step 1) and then substituting the ML estimate of the interference covariance matrix in place of the exact one (step 2)) is considered

$$\frac{\max\limits_{\substack{a, \\ |\Delta u| \leq \alpha\ |\Delta v| \leq \beta}} f_{\mathcal{H}_1}(\boldsymbol{r} | \boldsymbol{M} = K^{-1}\boldsymbol{S}, a, \boldsymbol{\Delta\theta})}{f_{\mathcal{H}_0}(\boldsymbol{r} | \boldsymbol{M} = K^{-1}\boldsymbol{S})} \underset{\mathcal{H}_0}{\overset{\mathcal{H}_1}{\gtrless}} T_1, \tag{16}$$

[3]The developed model can be easily extended to control the array manifold approximation accuracy. Specifically, a set $\{(\bar{u}_i, \bar{v}_i)\}_{i=1}^{D}$ of reference look-directions can be considered together with the corresponding linearized models. Hence, the detection problem can be framed as a generalized union-of-subspace hypothesis test [40], [41], where each hypothesis corresponds to the non-convex set associated with a specific linearized model.

[4]With a slight abuse of notation, the same symbol is used to denote the detection threshold and its possible modifications introduced later, see, e.g., (18).

where

$$\boldsymbol{S} = \sum_{k=1}^{K} \boldsymbol{r}_k \boldsymbol{r}_k^{\dagger} \tag{17}$$

is proportional, via K, to the conventional secondary data sample covariance matrix. The motivation for considering both (15) and (16) stems from the observation that none of them can be a-priori claimed to be better than the other.

Following the same line of reasoning as in [19] and [20], it is not difficult to show that (15) and (16) can be cast respectively as

$$\max_{\substack{|\Delta u| \leq \alpha \\ |\Delta v| \leq \beta}} \frac{1}{1 + \boldsymbol{r}^{\dagger}\boldsymbol{S}^{-1}\boldsymbol{r}} \frac{\left|\boldsymbol{r}^{\dagger}\boldsymbol{S}^{-1}(\boldsymbol{p} + \boldsymbol{H}\boldsymbol{\Delta\theta})\right|^2}{(\boldsymbol{p} + \boldsymbol{H}\boldsymbol{\Delta\theta})^{\dagger}\boldsymbol{S}^{-1}(\boldsymbol{p} + \boldsymbol{H}\boldsymbol{\Delta\theta})} \underset{\mathcal{H}_0}{\overset{\mathcal{H}_1}{\gtrless}} T, \tag{18}$$

and

$$\max_{\substack{|\Delta u| \leq \alpha \\ |\Delta v| \leq \beta}} \frac{\left|\boldsymbol{r}^{\dagger}\boldsymbol{S}^{-1}(\boldsymbol{p} + \boldsymbol{H}\boldsymbol{\Delta\theta})\right|^2}{(\boldsymbol{p} + \boldsymbol{H}\boldsymbol{\Delta\theta})^{\dagger}\boldsymbol{S}^{-1}(\boldsymbol{p} + \boldsymbol{H}\boldsymbol{\Delta\theta})} \underset{\mathcal{H}_0}{\overset{\mathcal{H}_1}{\gtrless}} T_1. \tag{19}$$

Remarkably, once the presence of a target is declared, i.e., the decision statistic on left hand side of (18) exceeds the detection threshold T, its angular estimate is obtained as a by-product from the decision statistic computation (18) and (19). Note that the evaluation of the decision rule in (18) as well as in (19) involves a non-convex fractional quadratic optimization problem. To handle it, different solution techniques are now devised, which represent the main technical contribution of this work from an optimization theory point of view. The 1-D case is studied in Subsection III-A whereas the 2-D case is analyzed in Subsection III-B. Before proceeding further, it is worth observing that the decision statistic in (18) is upper bounded by

$$\hat{t}_{upper}(\boldsymbol{r}, \boldsymbol{S}) = \max_{\boldsymbol{\Delta\theta} \in \mathbb{C}^2} \frac{1}{1 + \boldsymbol{r}^{\dagger}\boldsymbol{S}^{-1}\boldsymbol{r}} \frac{\left|\boldsymbol{r}^{\dagger}\boldsymbol{S}^{-1}(\boldsymbol{p} + \boldsymbol{H}\boldsymbol{\Delta\theta})\right|^2}{\left|\boldsymbol{S}^{-1/2}(\boldsymbol{p} + \boldsymbol{H}\boldsymbol{\Delta\theta})\right|^2} =$$
$$= \frac{\boldsymbol{r}^{\dagger}\boldsymbol{S}^{-1}\boldsymbol{H}_{SD}\left(\boldsymbol{H}_{SD}^{\dagger}\boldsymbol{S}^{-1}\boldsymbol{H}_{SD}\right)^{-1}\boldsymbol{H}_{SD}^{\dagger}\boldsymbol{S}^{-1}\boldsymbol{r}}{1 + \boldsymbol{r}^{\dagger}\boldsymbol{S}^{-1}\boldsymbol{r}},$$

with $\boldsymbol{H}_{SD} = [\boldsymbol{p}, \boldsymbol{H}]$, namely,

$$\max_{\substack{|\Delta u| \leq \alpha \\ |\Delta v| \leq \beta}} \frac{1}{1 + \boldsymbol{r}^{\dagger}\boldsymbol{S}^{-1}\boldsymbol{r}} \frac{\left|\boldsymbol{r}^{\dagger}\boldsymbol{S}^{-1}(\boldsymbol{p} + \boldsymbol{H}\boldsymbol{\Delta\theta})\right|^2}{\left|\boldsymbol{S}^{-1/2}(\boldsymbol{p} + \boldsymbol{H}\boldsymbol{\Delta\theta})\right|^2} < \hat{t}_{upper}(\boldsymbol{r}, \boldsymbol{S}). \tag{20}$$

Being the probability density function of $\hat{t}_{upper}(\boldsymbol{r}, \boldsymbol{S})$, under the $\mathcal{H}_0$ hypothesis, functionally independent of $\boldsymbol{M}$, it follows that the decision rule in (18) ensures the bounded Constant False Alarm Rate (CFAR) property. Indeed, for any given upper bound to the desired false alarm probability, a universal threshold, namely, just depending on the system parameters (i.e., pointing direction, number of antennas, and sample support size), can be set in (18) to fulfill the upper bound constraint. Leveraging (20), this property holds true even if a sub-optimal maximization is performed in (18) and thus an approximated implementation of the decision statistic in (18) is considered. Finally, following the same line of reasoning as

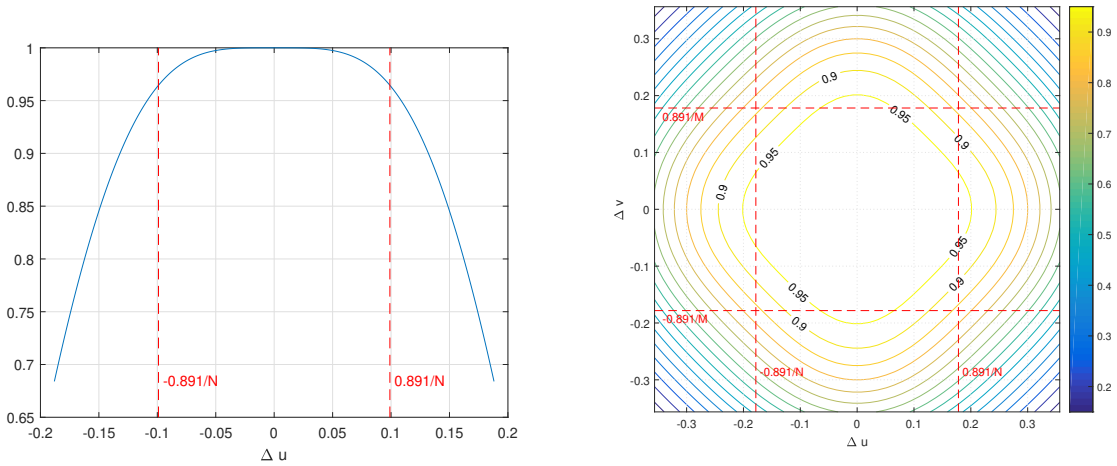

(a) (b)

Fig. 2. Normalized correlation versus direction cosine offset, assuming symmetric array: (a) 1-D case with $N = 9$ and $\bar{u} = 0$; (b) 2-D case with $N = M = 5$ and $\bar{u} = \bar{v} = 0$. Dashed red lines delimitate the 3 dB beamwidth.

before, it is not difficult to show that the two-step detector (19) and its possible sub-optimal implementations, i.e., relying on sub-optimal solution techniques to handle the involved maximization problem, still exhibit the bounded CFAR property.

A. Constrained GLRT Detector for 1-D Scenario

Handling the optimization problem involved in (18) and (19) for the 1-D case is tantamount to solving

$$\max_{|\Delta u|\leq\alpha} \frac{(\boldsymbol{p}+\dot{\boldsymbol{p}}_u\Delta u)^\dagger \boldsymbol{S}^{-1}\boldsymbol{r}\,\boldsymbol{r}^\dagger \boldsymbol{S}^{-1}(\boldsymbol{p}+\dot{\boldsymbol{p}}_u\Delta u)}{(\boldsymbol{p}+\dot{\boldsymbol{p}}_u\Delta u)^\dagger \boldsymbol{S}^{-1}(\boldsymbol{p}+\dot{\boldsymbol{p}}_u\Delta u)}. \tag{21}$$

In order to proceed, let us define the "whitened" quantities

$$\bar{\boldsymbol{p}} = \boldsymbol{S}^{-1/2}\boldsymbol{p}, \quad \dot{\bar{\boldsymbol{p}}}_u = \boldsymbol{S}^{-1/2}\dot{\boldsymbol{p}}_u, \quad \bar{\boldsymbol{r}} = \boldsymbol{S}^{-1/2}\boldsymbol{r}, \tag{22}$$

and recast Problem (21) as

$$\max_{|\Delta u|\leq\alpha} \frac{(\bar{\boldsymbol{p}}+\dot{\bar{\boldsymbol{p}}}_u\Delta u)^\dagger \bar{\boldsymbol{r}}\,\bar{\boldsymbol{r}}^\dagger (\bar{\boldsymbol{p}}+\dot{\bar{\boldsymbol{p}}}_u\Delta u)}{(\bar{\boldsymbol{p}}+\dot{\bar{\boldsymbol{p}}}_u\Delta u)^\dagger (\bar{\boldsymbol{p}}+\dot{\bar{\boldsymbol{p}}}_u\Delta u)}. \tag{23}$$

The following proposition establishes a procedure to obtain a closed-form optimal solution to (23).

Proposition 1. *An optimal solution $\Delta u^\star$ to (23) is*

$$\Delta u^\star = \underset{\Delta u\in\{\Delta u_1,\Delta u_2\}\cup\mathcal{B}}{\arg\max} \frac{(\bar{\boldsymbol{p}}+\dot{\bar{\boldsymbol{p}}}_u\Delta u)^\dagger \bar{\boldsymbol{r}}\,\bar{\boldsymbol{r}}^\dagger (\bar{\boldsymbol{p}}+\dot{\bar{\boldsymbol{p}}}_u\Delta u)}{(\bar{\boldsymbol{p}}+\dot{\bar{\boldsymbol{p}}}_u\Delta u)^\dagger (\bar{\boldsymbol{p}}+\dot{\bar{\boldsymbol{p}}}_u\Delta u)}, \tag{24}$$

where $\Delta u_i = (-1)^i\,\alpha, \quad i = 1, 2$, and $\mathcal{B}$ is the finite set (whose cardinality is at most 2) containing the real roots (with absolute value less than α) of the quadratic equation

$$a'\Delta u^2 + b'\Delta u + c' = 0, \tag{25}$$

with

$$a' = \left|\bar{\boldsymbol{r}}^\dagger\dot{\bar{\boldsymbol{p}}}_u\right|^2 \mathrm{Re}\{\bar{\boldsymbol{p}}^\dagger\dot{\bar{\boldsymbol{p}}}_u\} - \|\dot{\bar{\boldsymbol{p}}}_u\|^2 \mathrm{Re}\{\bar{\boldsymbol{p}}^\dagger\bar{\boldsymbol{r}}\,\bar{\boldsymbol{r}}^\dagger\dot{\bar{\boldsymbol{p}}}_u\}, \tag{26}$$

$$b' = \|\bar{\boldsymbol{p}}\|^2 \left|\bar{\boldsymbol{r}}^\dagger\dot{\bar{\boldsymbol{p}}}_u\right|^2 - \|\dot{\bar{\boldsymbol{p}}}_u\|^2 \left|\bar{\boldsymbol{r}}^\dagger\bar{\boldsymbol{p}}\right|^2, \tag{27}$$

$$c' = \|\bar{\boldsymbol{p}}\|^2 \mathrm{Re}\{\bar{\boldsymbol{p}}^\dagger\bar{\boldsymbol{r}}\,\bar{\boldsymbol{r}}^\dagger\dot{\bar{\boldsymbol{p}}}_u\} - \left|\bar{\boldsymbol{r}}^\dagger\bar{\boldsymbol{p}}\right|^2 \mathrm{Re}\{\bar{\boldsymbol{p}}^\dagger\dot{\bar{\boldsymbol{p}}}_u\}. \tag{28}$$

Proof: the interested reader may refer to Appendix B of the supplementary material to this paper. ■

Exploiting the above results, it follows that the decision rule (18) for the 1-D case, referred to in the following as GLRT for Linearized Array Manifold (GLRT-LAM), can be expressed in closed form as

$$t_{\text{GLRT-LAM}} = \frac{1}{1+\|\bar{\boldsymbol{r}}\|^2} \frac{\left|\bar{\boldsymbol{r}}^\dagger(\bar{\boldsymbol{p}}+\dot{\bar{\boldsymbol{p}}}_u\widehat{\Delta u}^\star)\right|^2}{\left\|\bar{\boldsymbol{p}}+\dot{\bar{\boldsymbol{p}}}_u\widehat{\Delta u}^\star\right\|^2} \underset{\mathcal{H}_0}{\overset{\mathcal{H}_1}{\gtrless}} T, \tag{29}$$

where $\widehat{\Delta u}^\star$ is given by Proposition 1 (therein denoted by $\Delta u^\star$) and represents the output estimate of the target DOA displacement, provided that a detection is declared. The computational complexity required to implement the GLRT-LAM is $\mathcal{O}(KN^2)$, namely it is dominated by Sample Covariance Matrix (SCM) evaluation. Finally. the AMF counterpart to (29), denoted as GLRT-LAM-AMF, is given by

$$t_{\text{GLRT-LAM-AMF}} = \frac{\left|\bar{\boldsymbol{r}}^\dagger(\bar{\boldsymbol{p}}+\dot{\bar{\boldsymbol{p}}}_u\widehat{\Delta u}^\star)\right|^2}{\left\|\bar{\boldsymbol{p}}+\dot{\bar{\boldsymbol{p}}}_u\widehat{\Delta u}^\star\right\|^2} \underset{\mathcal{H}_0}{\overset{\mathcal{H}_1}{\gtrless}} T_1, \tag{30}$$

B. Constrained GLRT Detector for 2-D Scenario

For the 2-D array sensing scenario, the optimization problem to solve boils down to

$$\max_{\substack{|\Delta u|\leq\alpha\\|\Delta v|\leq\beta}} \frac{(\boldsymbol{p}+\boldsymbol{H}\boldsymbol{\Delta\theta})^\dagger \boldsymbol{S}^{-1}\boldsymbol{r}\,\boldsymbol{r}^\dagger \boldsymbol{S}^{-1}(\boldsymbol{p}+\boldsymbol{H}\boldsymbol{\Delta\theta})}{(\boldsymbol{p}+\boldsymbol{H}\boldsymbol{\Delta\theta})^\dagger \boldsymbol{S}^{-1}(\boldsymbol{p}+\boldsymbol{H}\boldsymbol{\Delta\theta})}, \tag{31}$$

which can be equivalently expressed as

$$\max_{\substack{|\Delta u|\leq\alpha\\|\Delta v|\leq\beta}} \frac{(\bar{\boldsymbol{p}}+\bar{\boldsymbol{H}}\boldsymbol{\Delta\theta})^\dagger \bar{\boldsymbol{r}}\,\bar{\boldsymbol{r}}^\dagger (\bar{\boldsymbol{p}}+\bar{\boldsymbol{H}}\boldsymbol{\Delta\theta})}{(\bar{\boldsymbol{p}}+\bar{\boldsymbol{H}}\boldsymbol{\Delta\theta})^\dagger (\bar{\boldsymbol{p}}+\bar{\boldsymbol{H}}\boldsymbol{\Delta\theta})}, \tag{32}$$

where $\bar{\boldsymbol{p}}$ and $\bar{\boldsymbol{r}}$ are defined in (22), whereas $\bar{\boldsymbol{H}}$ is given by

$$\bar{\boldsymbol{H}} = \boldsymbol{S}^{-1/2}\boldsymbol{H}. \tag{33}$$

In the following, two optimization procedures are considered to handle Problem (32), which allow to localize the target within the antenna beam if its presence is declared. The former reaches the global optimum via the Dinkelbach algorithm [33]. The latter relies on a CD method [42] and converges to a stationary point without any theoretical guarantee to end up in a global maximizer of Problem (32). The second possibly sub-optimal approach exhibits in general a faster convergence than the Dinkelbach-based procedure, which can be a valuable feature from a practical point of view.

1) Dinkelbach-based DOA displacements estimate: To obtain the global optimal solution to Problem (32) some results from the fractional programming theory [33], [34], [35] are exploited, which are summarized here in the form of a lemma.

Lemma III.1. [33] *Consider the fractional programming problem*

$$\max_{\boldsymbol{x}\in\mathcal{S}} Q(\boldsymbol{x}) = N(\boldsymbol{x})/D(\boldsymbol{x}), \tag{34}$$

where $\mathcal{S} \subseteq \mathbb{R}^n$ is a nonempty and compact set and $N(\boldsymbol{x}), D(\boldsymbol{x}) : \mathcal{S} \to \mathbb{R}$ are continuous functions, with $D(\boldsymbol{x})$ strictly positive. Then $\boldsymbol{x}^\star$ is an optimal solution to (34) if and only if it maximizes

$$N(\boldsymbol{x}) - Q(\boldsymbol{x}^\star)D(\boldsymbol{x}). \tag{35}$$

Furthermore, the function

$$F(q) = \max_{\boldsymbol{x}\in\mathcal{S}} \; N(\boldsymbol{x}) - qD(\boldsymbol{x}), \quad q \in \mathbb{R}. \tag{36}$$

is continuous, convex, and strictly decreasing on $\mathbb{R}$ with $F(q) > 0$ if $q < q^\star = Q(\boldsymbol{x}^\star)$ and $F(q) < 0$ if $q > q^\star$. ■

Based on Lemma III.1, an optimal solution to (34) can be found determining the unique root of (36), possibly via the bisection method, and computing the corresponding maximizer. This procedure, proposed by Dinkelbach [33], is summarized in **Algorithm 1**. Evidently, Problem (32) fulfils the conditions of Lemma III.1 with

$$\boldsymbol{x} = \boldsymbol{\Delta\theta} \in \mathbb{R}^2, \tag{37}$$

$$N(\boldsymbol{x}) = (\bar{\boldsymbol{p}} + \bar{\boldsymbol{H}}\boldsymbol{x})^\dagger \, \bar{\boldsymbol{r}} \, \bar{\boldsymbol{r}}^\dagger \, (\bar{\boldsymbol{p}} + \bar{\boldsymbol{H}}\boldsymbol{x}), \tag{38}$$

$$D(\boldsymbol{x}) = (\bar{\boldsymbol{p}} + \bar{\boldsymbol{H}}\boldsymbol{x})^\dagger \, (\bar{\boldsymbol{p}} + \bar{\boldsymbol{H}}\boldsymbol{x}), \tag{39}$$

and

$$\mathcal{S} = \{\boldsymbol{x} \in \mathbb{R}^2 : |\boldsymbol{x}(1)| \leq \alpha, |\boldsymbol{x}(2)| \leq \beta\}. \tag{40}$$

In fact, the feasible set (40) is nonempty and compact, (38) and (39) are continuous functions with (39) strictly[5] greater than zero over $\mathcal{S}$. As a result, **Algorithm 1** can be applied to solve Problem (32), where step 4 becomes

$$\begin{aligned}\boldsymbol{\Delta\theta}_n^\star = \underset{\boldsymbol{\Delta\theta}\,\in\,\mathcal{S}}{\arg\max} \; & (\bar{\boldsymbol{p}} + \bar{\boldsymbol{H}}\boldsymbol{\Delta\theta})^\dagger \, \bar{\boldsymbol{r}} \, \bar{\boldsymbol{r}}^\dagger \, (\bar{\boldsymbol{p}} + \bar{\boldsymbol{H}}\boldsymbol{\Delta\theta}) \\ & - q_n \, (\bar{\boldsymbol{p}} + \bar{\boldsymbol{H}}\boldsymbol{\Delta\theta})^\dagger \, (\bar{\boldsymbol{p}} + \bar{\boldsymbol{H}}\boldsymbol{\Delta\theta}).\end{aligned} \tag{41}$$

The procedure devised to determine an optimal point $\boldsymbol{\Delta\theta}_n^\star$ is summarized in **Algorithm 2** (analytical details are reported in Appendix C of the supplementary material to this paper). Specifically, in step 2 the candidate optimal solutions that lie within the interior of the feasible set are determined. Besides, in steps 3 and 4 the candidate optimal solutions belonging to the boundary of the feasible set, i.e., the four edges of the box, are computed. Finally, Step 5 derives the global optimal solution, selecting the best among all the obtained candidates.

Note that $F(0) > 0$ and $F(\|\bar{\boldsymbol{r}}\|^2) < 0$ with probability one[6] provided that $NM > 3$. As a consequence, the bisection method involved in **Algorithm 1** can be initialized with $q_{lb} = 0$ and $q_{ub} = \|\bar{\boldsymbol{r}}\|^2$ to solve Problem (32).

Algorithm 1 Dinkelbach's Optimization Algorithm

Input: $\mathcal{S} \subseteq \mathbb{R}^n$, $N(\boldsymbol{x})$, $D(\boldsymbol{x})$, q_{ub}, q_{lb} and ε_{DO}.
Output: A solution $\boldsymbol{x}^\star$ to (34).

1: set $n = 0$.
2: **do**
3: $\quad q_n = (q_{lb} + q_{ub})/2$;
4: $\quad$ find $\boldsymbol{x}_n^\star = \arg\max_{\boldsymbol{x}\in\mathcal{S}}\{N(\boldsymbol{x}) - q_n D(\boldsymbol{x})\}$;
5: $\quad$ let $F(q_n) = \{N(\boldsymbol{x}_n^\star) - q_n D(\boldsymbol{x}_n^\star)\}$;
6: $\quad$ **if** $F(q_n) \geq 0$ set $q_{lb} = q_n$, otherwise $q_{ub} = q_n$;
7: $\quad n = n + 1$;
8: **until** $F(q_n) = 0$ or $(q_{ub} - q_{lb})/2 < \varepsilon_{DO}$
9: output $\boldsymbol{x}^\star = \boldsymbol{x}_n^\star$.

Now, denoting by $\widehat{\Delta}\boldsymbol{\theta}_{DO}^\star$ the DOA displacements estimated via **Algorithm 1** tailored to the problem at hand, the decision rule (18) becomes

$$t_{\text{GLRT-LAM-DO}} = \frac{1}{1 + \|\bar{\boldsymbol{r}}\|^2} \frac{\left|\bar{\boldsymbol{r}}^\dagger(\bar{\boldsymbol{p}} + \bar{\boldsymbol{H}}\widehat{\Delta}\boldsymbol{\theta}_{DO}^\star)\right|^2}{\left\|\bar{\boldsymbol{p}} + \bar{\boldsymbol{H}}\widehat{\Delta}\boldsymbol{\theta}_{DO}^\star\right\|^2} \underset{\mathcal{H}_0}{\overset{\mathcal{H}_1}{\gtrless}} T, \tag{42}$$

which will be denoted hereafter as GLRT-LAM with Dinkelbach Optimization (GLRT-LAM-DO). Finally, the AMF version of (42), referred to as GLRT-LAM-DO-AMF, is given by

$$t_{\text{GLRT-LAM-DO-AMF}} = \frac{\left|\bar{\boldsymbol{r}}^\dagger(\bar{\boldsymbol{p}} + \bar{\boldsymbol{H}}\widehat{\Delta}\boldsymbol{\theta}_{DO}^\star)\right|^2}{\left\|\bar{\boldsymbol{p}} + \bar{\boldsymbol{H}}\widehat{\Delta}\boldsymbol{\theta}_{DO}^\star\right\|^2} \underset{\mathcal{H}_0}{\overset{\mathcal{H}_1}{\gtrless}} T_1. \tag{43}$$

GLRT-LAM-DO and GLRT-LAM-DO-AMF involve $\mathcal{O}(K(NM)^2 + N_{it,b})$ operations, where $N_{it,b}$ is the number of iterations required by the bisection algorithm to converge. In fact, the complexity of the SCM inverse computation is $\mathcal{O}(K(NM)^2)$ and $\mathcal{O}(1)$ operations are necessary at each execution of **Algorithm 2**.

[5] Note that the vectors in (9) and (10) can be re-written as $\dot{\boldsymbol{p}}_u = \boldsymbol{p}(\bar{u}, \bar{v}) \odot \boldsymbol{v}_u$, and $\dot{\boldsymbol{p}}_v = \boldsymbol{p}(\bar{u}, \bar{v}) \odot \boldsymbol{v}_v$ respectively, where $\boldsymbol{v}_u = j\frac{2\pi}{\lambda_0}[x_0, x_1, \ldots, x_{N-1}]^T \otimes \boldsymbol{1}_M$ and $\boldsymbol{v}_v = j\frac{2\pi}{\lambda_0}\boldsymbol{1}_N \otimes [y_0, y_1, \ldots, y_{M-1}]^T$. Being $\boldsymbol{S}^{-1} \succ 0$, $D(\boldsymbol{x}) = 0$ if and only if $\bar{\boldsymbol{p}} + \bar{\boldsymbol{H}}\boldsymbol{x} = \boldsymbol{0}$, namely $\boldsymbol{p}(\bar{u}, \bar{v}) \odot (\boldsymbol{1}_{NM} + \xi\boldsymbol{v}_u - \chi\boldsymbol{v}_v) = \boldsymbol{0}$, with $\xi, \chi \in \mathbb{R}$. Being $\boldsymbol{p}(\bar{u}, \bar{v})$ unimodular, this is tantamount to $(\boldsymbol{1}_{NM} + \xi\boldsymbol{v}_u - \chi\boldsymbol{v}_v) = \boldsymbol{0}, \quad \xi, \chi \in \mathbb{R}$, which is impossible because $\text{Re}\{\boldsymbol{1}_{NM} + \xi\boldsymbol{v}_u - \beta\boldsymbol{v}_v\} = \boldsymbol{1}_{NM} \; \forall \xi, \chi \in \mathbb{R}$.

[6] Both $F(0) = \arg\max_{\boldsymbol{\Delta\theta}\,\in\,\mathcal{S}} \|\bar{\boldsymbol{r}}^\dagger(\bar{\boldsymbol{p}} + \bar{\boldsymbol{H}}\boldsymbol{\Delta\theta})\|^2 = 0$ and $F(\|\bar{\boldsymbol{r}}\|^2) = \arg\max_{\boldsymbol{\Delta\theta}\,\in\,\mathcal{S}} \|\bar{\boldsymbol{r}}^\dagger(\bar{\boldsymbol{p}} + \bar{\boldsymbol{H}}\boldsymbol{\Delta\theta})\|^2 - \|\bar{\boldsymbol{r}}\|^2\|\bar{\boldsymbol{p}} + \bar{\boldsymbol{H}}\boldsymbol{\Delta\theta}\|^2 = 0$ force $\bar{\boldsymbol{r}}$ to lie in a specific subspace whose dimension is less than NM. This is an event that occurs with zero probability.

Algorithm 2 Solution to Problem (41)

Input: $\bar{\boldsymbol{r}}, \bar{\boldsymbol{p}}, \dot{\bar{\boldsymbol{p}}}_u, \dot{\bar{\boldsymbol{p}}}_v, q_n, \alpha, \beta$.
Output: A solution $\boldsymbol{\Delta\theta}_n^\star$ to (41).

1: let $\mathcal{V} = \varnothing$;
2: compute the unconstrained stationary point $\boldsymbol{\Delta\theta}_1$ of (41) (see equation (57) reported in the supplementary material to this paper) and set
$$\mathcal{V} = \mathcal{V} \cup \{\boldsymbol{\Delta\theta}_1\} \cap \mathcal{S};$$
3: restrict the objective of (41) to the right (left) edge of $\mathcal{S}$, i.e., $\Delta u = \alpha$ ($\Delta u = -\alpha$), and compute the corresponding stationary point $\boldsymbol{\Delta\theta}_2$ ($\boldsymbol{\Delta\theta}_3$) (see equation (65) reported in the supplementary material to this paper); hence, set
$$\mathcal{V} = \mathcal{V} \cup \{\boldsymbol{\Delta\theta}_2, \boldsymbol{\Delta\theta}_3\};$$
4: restrict the objective of (41) to the upper (lower) edge of $\mathcal{S}$, i.e., $\Delta v = \beta$ ($\Delta v = -\beta$), and compute the corresponding stationary point $\boldsymbol{\Delta\theta}_4$ ($\boldsymbol{\Delta\theta}_5$) (see equation (66) reported in the supplementary material to this paper); hence, set
$$\mathcal{V} = \mathcal{V} \cup \{\boldsymbol{\Delta\theta}_4, \boldsymbol{\Delta\theta}_5\};$$
5:
$$\boldsymbol{\Delta\theta}_n^\star = \underset{\boldsymbol{\Delta\theta} \in \mathcal{V}}{\arg\max}\ N(\boldsymbol{\Delta\theta}) - q_n D(\boldsymbol{\Delta\theta}),$$
where $N(\boldsymbol{\Delta\theta})$ and $D(\boldsymbol{\Delta\theta})$ are given in (38) and (39), respectively, and $\mathcal{V}$ is a set with cardinality at most 5;
6: output $\boldsymbol{\Delta\theta}_n^\star$.

Algorithm 3 Coordinate Descent Optimization Algorithm

Input: $\bar{\boldsymbol{r}}, \bar{\boldsymbol{p}}, \dot{\bar{\boldsymbol{p}}}_u, \dot{\bar{\boldsymbol{p}}}_v, q_n, \alpha, \beta, \varepsilon_{CDO}$.
Output: A solution $\widehat{\Delta\boldsymbol{\theta}}_{CDO}^\star$ to Problem (32).

1: set $n = 0$, $\boldsymbol{\Delta\theta}^{(n)} = [\Delta u^{(n)}, \Delta v^{(n)}]^T = \mathbf{0}$,
$\bar{\boldsymbol{p}}_{\Delta v}^{(n)} = \bar{\boldsymbol{p}} + \dot{\bar{\boldsymbol{p}}}_v \Delta v^{(n)}$,
$\text{obj}^{(n)} = \dfrac{(\bar{\boldsymbol{p}} + \bar{\boldsymbol{H}}\boldsymbol{\Delta\theta}^{(n)})^\dagger\, \bar{\boldsymbol{r}}\, \bar{\boldsymbol{r}}^\dagger\, (\bar{\boldsymbol{p}} + \bar{\boldsymbol{H}}\boldsymbol{\Delta\theta}^{(n)})}{(\bar{\boldsymbol{p}} + \bar{\boldsymbol{H}}\boldsymbol{\Delta\theta}^{(n)})^\dagger\, (\bar{\boldsymbol{p}} + \bar{\boldsymbol{H}}\boldsymbol{\Delta\theta}^{(n)})}$;
2: **repeat**
3: $n = n + 1$;
4: Δu optimization, i.e.,
$$\Delta u^\star = \underset{|\Delta u| \le \alpha}{\arg\max} \frac{(\bar{\boldsymbol{p}}_{\Delta v}^{(n-1)} + \dot{\bar{\boldsymbol{p}}}_u \Delta u)^\dagger \bar{\boldsymbol{r}}\, \bar{\boldsymbol{r}}^\dagger (\bar{\boldsymbol{p}}_{\Delta v}^{(n-1)} + \dot{\bar{\boldsymbol{p}}}_u \Delta u)}{(\bar{\boldsymbol{p}}_{\Delta v}^{(n-1)} + \dot{\bar{\boldsymbol{p}}}_u \Delta u)^\dagger (\bar{\boldsymbol{p}}_{\Delta v}^{(n-1)} + \dot{\bar{\boldsymbol{p}}}_u \Delta u)},$$
and set $\bar{\boldsymbol{p}}_{\Delta u}^{(n)} = \bar{\boldsymbol{p}} + \dot{\bar{\boldsymbol{p}}}_u \Delta u^\star$;
5: Δv optimization, i.e.,
$$\Delta v^\star = \underset{|\Delta v| \le \beta}{\arg\max} \frac{(\bar{\boldsymbol{p}}_{\Delta u}^{(n)} + \dot{\bar{\boldsymbol{p}}}_v \Delta v)^\dagger \bar{\boldsymbol{r}}\, \bar{\boldsymbol{r}}^\dagger (\bar{\boldsymbol{p}}_{\Delta u}^{(n)} + \dot{\bar{\boldsymbol{p}}}_v \Delta v)}{(\bar{\boldsymbol{p}}_{\Delta u}^{(n)} + \dot{\bar{\boldsymbol{p}}}_v \Delta v)^\dagger (\bar{\boldsymbol{p}}_{\Delta u}^{(n)} + \dot{\bar{\boldsymbol{p}}}_v \Delta v)},$$
and set $\bar{\boldsymbol{p}}_{\Delta v}^{(n)} = \bar{\boldsymbol{p}} + \dot{\bar{\boldsymbol{p}}}_v \Delta v^\star$;
6: $\boldsymbol{\Delta\theta}^{(n)} = [\Delta u^\star, \Delta v^\star]^T$ and
$\text{obj}^{(n)} = \dfrac{(\bar{\boldsymbol{p}} + \bar{\boldsymbol{H}}\boldsymbol{\Delta\theta}^{(n)})^\dagger\, \bar{\boldsymbol{r}}\, \bar{\boldsymbol{r}}^\dagger\, (\bar{\boldsymbol{p}} + \bar{\boldsymbol{H}}\boldsymbol{\Delta\theta}^{(n)})}{(\bar{\boldsymbol{p}} + \bar{\boldsymbol{H}}\boldsymbol{\Delta\theta}^{(n)})^\dagger\, (\bar{\boldsymbol{p}} + \bar{\boldsymbol{H}}\boldsymbol{\Delta\theta}^{(n)})}$;
7: **until** $|\text{obj}^{(n)} - \text{obj}^{(n-1)}| < \varepsilon_{CDO}$
8: output $\widehat{\Delta\boldsymbol{\theta}}_{CDO}^\star = \boldsymbol{\Delta\theta}^{(n)}$.

2) Coordinate Descent DOA displacements estimate: Exploiting the CD framework, in this subsection another method is proposed to handle Problem (32). The idea is to alternate between the maximizations over each entry of $\boldsymbol{\Delta\theta} = [\Delta u, \Delta v]^T$, namely optimizing one variable at a time while keeping the other fixed. Note that in the presence of two blocks/variables the alternating update rule involved in the CD approach is equivalent to the Maximum Block Improvement (MBI) policy [36]. As a result, any limit point of the sequence of solutions produced by the CD procedure is a stationary point for Problem (32). In **Algorithm 3**, the CD-based solution technique specific for Problem (32) is reported. Note that the optimizations required at steps 4 and 5 can be performed resorting to Proposition 1. Otherwise stated, closed-form optimal solutions are available. Leveraging the output $\widehat{\Delta\boldsymbol{\theta}}_{CDO}^\star$ of **Algorithm 3**, the following approximated versions of (42) and (43), referred to as GLRT-LAM with CD optimization (GLRT-LAM-CDO) and GLRT-LAM-CDO-AMF, are obtained

$$t_{\text{GLRT-LAM-CDO}} = \frac{1}{1 + \|\bar{\boldsymbol{r}}\|^2} \frac{\left|\bar{\boldsymbol{r}}^\dagger (\bar{\boldsymbol{p}} + \bar{\boldsymbol{H}}\widehat{\Delta\boldsymbol{\theta}}_{CDO}^\star)\right|^2}{\left\|\bar{\boldsymbol{p}} + \bar{\boldsymbol{H}}\widehat{\Delta\boldsymbol{\theta}}_{CDO}^\star\right\|^2} \underset{\mathcal{H}_0}{\overset{\mathcal{H}_1}{\gtrless}} T, \tag{44}$$

and

$$t_{\text{GLRT-LAM-CDO-AMF}} = \frac{\left|\bar{\boldsymbol{r}}^\dagger (\bar{\boldsymbol{p}} + \bar{\boldsymbol{H}}\widehat{\Delta\boldsymbol{\theta}}_{CDO}^\star)\right|^2}{\left\|\bar{\boldsymbol{p}} + \bar{\boldsymbol{H}}\widehat{\Delta\boldsymbol{\theta}}_{CDO}^\star\right\|^2} \underset{\mathcal{H}_0}{\overset{\mathcal{H}_1}{\gtrless}} T_1. \tag{45}$$

The implementation of GLRT-LAM-CDO and GLRT-LAM-CDO-AMF require $\mathcal{O}(K(NM)^2 + N_{it,CD})$ operations, where $N_{it,CD}$ denotes the number of iterations of the CD method up to convergence. Precisely $\mathcal{O}(K(NM)^2)$ are due to SCM and $\mathcal{O}(1)$ operations are necessary for each iteration of the CD method.

IV. Performance Analysis

This section is aimed at assessing the performance of the proposed strategies for joint target detection and angle estimation in comparison with some counterparts available in the open literature specifically designed either for detection or DOA evaluation. In the reported case studies the disturbance covariance matrix is modeled as $\boldsymbol{M} = \boldsymbol{M}_J + \sigma_a^2 \boldsymbol{I}$ where σ_a^2 is the white noise power level (assumed without loss of generality equal to 0 dB) and $\boldsymbol{M}_J$ refers to the jamming signals covariance contribution. Specifically, denoting by J_{NB} and J_{WB} the number of narrow-band and wide-band jammers, $\boldsymbol{M}_J = \boldsymbol{M}_1 + \boldsymbol{M}_2$, where

$$\boldsymbol{M}_1 = \sum_{j=1}^{J_{NB}} \sigma_j^2 \boldsymbol{p}_J(u_j, v_j) \boldsymbol{p}_J(u_j, v_j)^\dagger, \tag{46}$$

with $\boldsymbol{p}_J(u_j, v_j)$ the steering vector and σ_j^2 the power of the j-th jammer, while

$$\boldsymbol{M}_2 = \sum_{h=1}^{J_{WB}} \bar{\sigma}_h^2 \frac{1}{B_h} \int_{-\frac{B_h}{2}}^{\frac{B_h}{2}} \boldsymbol{p}_J(u_h, v_h) \boldsymbol{p}_J(u_h, v_h)^\dagger\, df \tag{47}$$

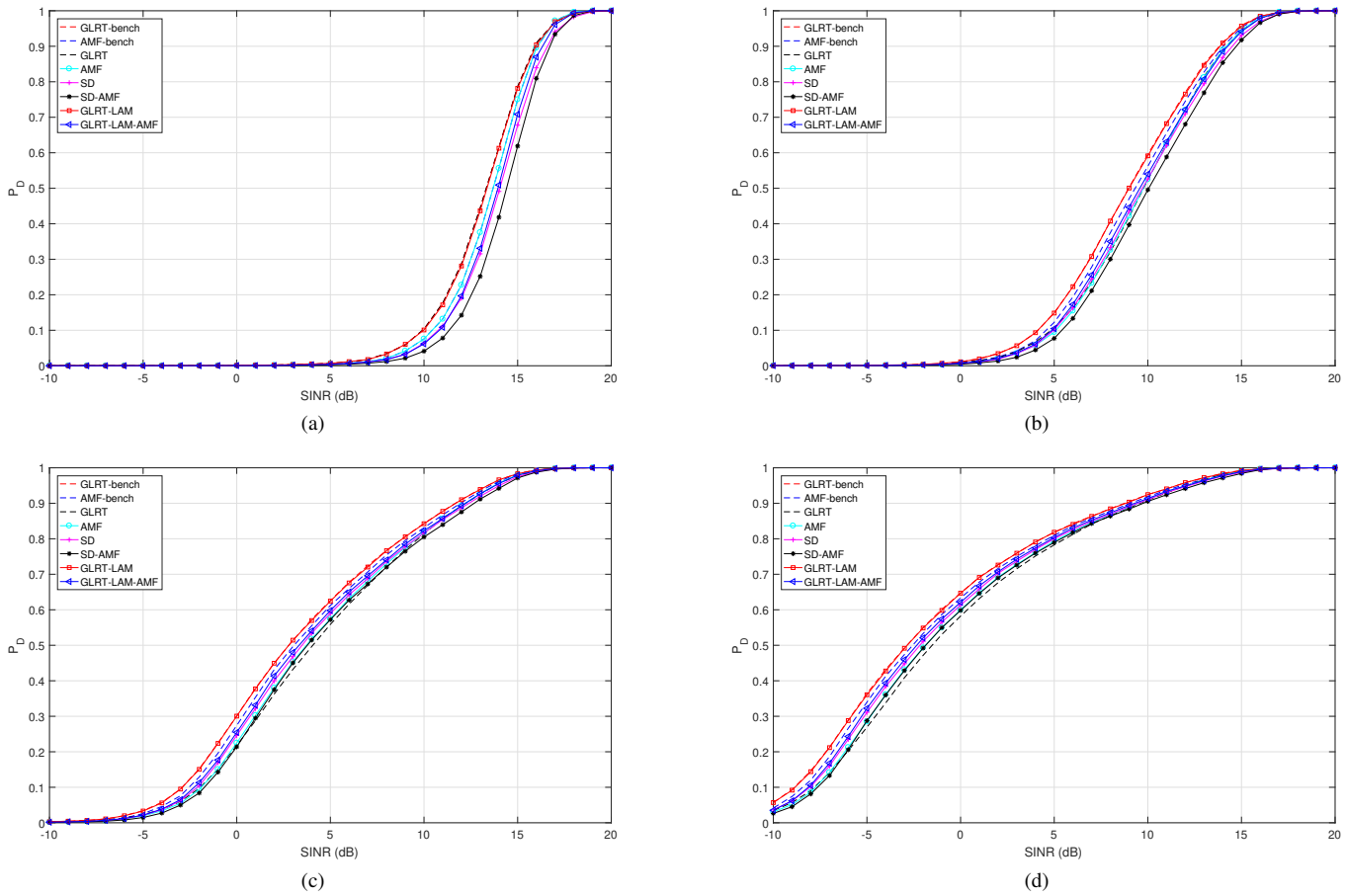

Fig. 3. Detection performance for a ULA with 16 antennas in Scenario 1 for different mismatches, assuming $K = 32$ and $\alpha = 0.5$. The actual DOA displacement is drawn from a uniform distribution over $[-\Delta, \Delta]$: (a) $\Delta = 0$, (b) $\Delta = 0.1$, (c) $\Delta = 0.25$, and (d) $\Delta = 0.5$.

with $\boldsymbol{p}_J(u_h, v_h)$, $\bar{\sigma}_h^2$, (u_h, v_h), and B_h, the steering vector, the power, the DOA parameters, and the actual bandwidth associated with the h-th interferer, respectively.

In the following, three different interfering environments are analyzed:

- Scenario 1: two narrow-band jammers located at $u_1 = v_1 = 0.1$ and $u_2 = v_2 = 0.3$, with Jammer to Noise Ratio (JNR) given by $JNR_1 = 30$ dB and $JNR_2 = 40$ dB, respectively ($\sigma_j^2 = JNR_j\, \sigma_a^2,\ j = 1, 2$).
- Scenario 2: one narrow-band jammer at $u_1 = v_1 = 0.1$, with $JNR_1 = 30$ dB ($\sigma_1^2 = JNR_1\, \sigma_a^2$), and one wide-band jammer ($B_f = 0.3$) at $u_2 = v_2 = 0.3$ with $JNR_2 = 40$ dB ($\bar{\sigma}_2^2 = JNR_2\, \sigma_a^2$).
- Scenario 3: two narrow-band jammers located at $u_1 = v_1 = 0.2$ and $u_2 = v_2 = 0.3$, with $JNR_1 = 30$ dB and $JNR_2 = 40$ dB, respectively ($\sigma_j^2 = JNR_j\, \sigma_a^2,\ j = 1, 2$)[7].

As already claimed, both detection and angle estimation capabilities of the proposed processors are analyzed. As to the former, the metric used to assess the performance is the Probability of Detection (P_D) estimated via standard Monte Carlo counting techniques over 10^4 independent trials. The threshold is set in order to guarantee a P_{fa} of 10^{-4} and it is evaluated using $100/P_{fa}$ independent trials. The decision statistics

$$t_{\text{GLRT}} = \frac{\left|\boldsymbol{r}^\dagger \boldsymbol{S}^{-1}\boldsymbol{p}\right|^2}{\left(1 + \boldsymbol{r}^\dagger \boldsymbol{S}^{-1}\boldsymbol{r}\right)\, \boldsymbol{p}^\dagger \boldsymbol{S}^{-1}\boldsymbol{p}},$$

$$t_{\text{AMF}} = \frac{\left|\boldsymbol{r}^\dagger \boldsymbol{S}^{-1}\boldsymbol{p}\right|^2}{\boldsymbol{p}^\dagger \boldsymbol{S}^{-1}\boldsymbol{p}},$$

$$t_{\text{SD}} = \frac{\boldsymbol{r}^\dagger \boldsymbol{S}^{-1}\boldsymbol{H}_{SD}\left(\boldsymbol{H}_{SD}^\dagger \boldsymbol{S}^{-1}\boldsymbol{H}_{SD}\right)^{-1}\boldsymbol{H}_{SD}^\dagger \boldsymbol{S}^{-1}\boldsymbol{r}}{1 + \boldsymbol{r}^\dagger \boldsymbol{S}^{-1}\boldsymbol{r}},$$

$$t_{\text{SD-AMF}} = \boldsymbol{r}^\dagger \boldsymbol{S}^{-1}\boldsymbol{H}_{SD}\left(\boldsymbol{H}_{SD}^\dagger \boldsymbol{S}^{-1}\boldsymbol{H}_{SD}\right)^{-1}\boldsymbol{H}_{SD}^\dagger \boldsymbol{S}^{-1}\boldsymbol{r},$$

referred to as GLRT [19], AMF [20], SD [21], and SD-AMF [18], [37], respectively, are considered for comparison purposes. GLRT and AMF detectors consider the nominal steering vector $\boldsymbol{p}$ as useful signal directions (they usually operate in mismatched conditions and are thus also referred to as mismatched detectors), while SD and SD-AMF assume as useful signal directions those given by the columns of $\boldsymbol{H}_{SD}$. Finally, to assess the limits of the proposed algorithms, the GLRT and the AMF receivers with a perfect knowledge of the target DOA parameters (indicated as GLRT-bench and AMF-bench, respectively) are included as benchmarks.

In regard to the estimation performance, the Mean Square

[7]Note that other interfering environments have also been considered confirming the general performance behavior shown in the next two sub-sections. The results are not reported for obvious reasons of brevity.

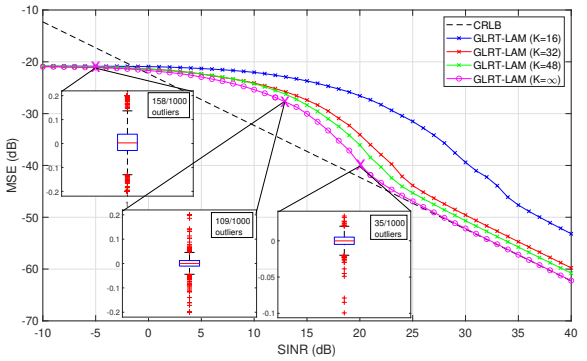

(a)

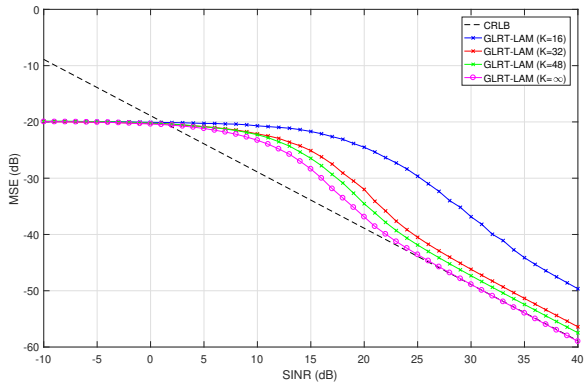

(b)

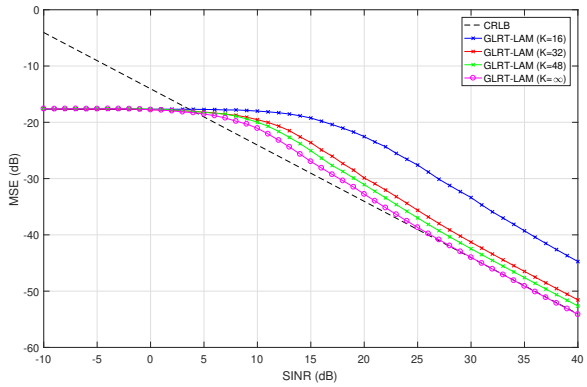

(c)

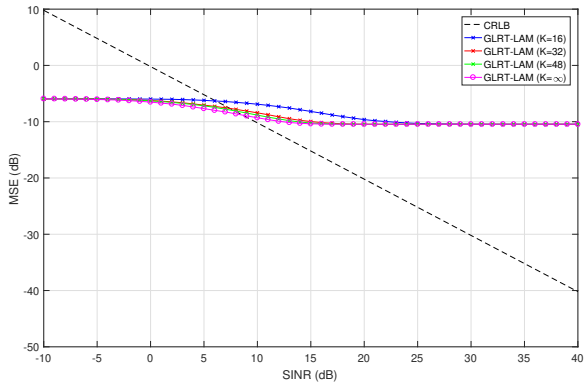

(d)

Fig. 4. Estimation performance for a ULA with 16 antennas in Scenario 1 assuming $\alpha = 0.2$ and considering different sample support sizes, i.e., $K = [16, 32, 48, \infty]$, and several target locations: (a) $\Delta u = 0$, (b) $\Delta u = 0.05$, (c) $\Delta u = 0.1$, and (d) $\Delta u = 0.5$.

Error (MSE) is considered as the figure of merit. Again, Monte Carlo counting techniques are used to compute the MSE as

$$\widehat{\text{MSE}} = \frac{1}{M_C} \sum_{i=1}^{M_C} \left\| \boldsymbol{\Delta\theta}_0 - \widehat{\Delta\boldsymbol{\theta}}_i \right\|^2, \tag{48}$$

where $M_C = 10^4$ indicates the number of Monte Carlo independent trials, $\boldsymbol{\Delta\theta}_0 \in \mathbb{R}^2$ is the actual DOA displacements vector and $\widehat{\Delta\boldsymbol{\theta}}_i$ refers to the estimate provided at the i-th trial by a given technique. As performance benchmark, the CRLB for DOA displacements (the interested reader may refer to Appendix D of the supplementary material to this paper) is reported too.

Two different simulation setups are considered in the following subsections to shed light on the performance limit of the proposed radar processors: a) linearized array manifold signal model; b) actual array manifold. Finally, the Signal to Interference plus Noise Ratio (SINR) is defined as

$$\text{SINR} = |a|^2 \boldsymbol{p}^\dagger \boldsymbol{M}^{-1} \boldsymbol{p}. \tag{49}$$

A. Linearized Array Manifold Signal Model

The performance of a radar system equipped with either a 1-D or a 2-D array pointing at the boresight direction is studied. The former employs a Uniform Linear Array (ULA) with $N = 16$ and $d_x = \lambda_0/2$. The latter exploits a URA with $N = M = 5$ and $d_x = d_y = \lambda_0/2$; in both cases the reference system is centered at the bottom-left corner. Within this subsection, the data from the cell under test are modeled as

$$\boldsymbol{r} = a\left(\boldsymbol{p} + \dot{\boldsymbol{p}}_u \Delta u + \dot{\boldsymbol{p}}_v \Delta v\right) + \boldsymbol{n}, \tag{50}$$

namely according to the linearized array manifold[8], in order to assess the capabilities of the devised signal processing techniques under nominal design conditions.

Fig. 3 shows the P_D curves for the 1-D case, assuming the interference environment of Scenario 1, with $K = 2N = 32$ secondary data. Therein, the design parameter α is set at 0.5. The actual DOA displacement is drawn from a uniform distribution over $[-\Delta, \Delta]$ and each subfigure refers to a specific value of Δ. Specifically, Fig. 3(a) considers $\Delta = 0$, i.e., the target is exactly matched to the array pointing direction, whereas Figs. 3(b), 3(c), and 3(d), consider $\Delta = 0.1, 0.25$, and 0.5, respectively.

Inspection of the figures highlights that the GLRT-LAM detector exhibits performance very close to the GLRT-bench and outperforms all the other counterparts (including the AMF-bench) regardless of the operating conditions. Besides, GLRT-LAM-AMF experiences a performance degradation (about 0.5 dB at $P_D = 0.9$, in the worst case) with respect to the corresponding benchmark. However, it achieves higher P_D levels than the mismatched detectors (of course apart from the case of $\Delta = 0$) and the subspace receivers in all the configurations, revealing the effectiveness of the method to estimate the actual steering vector.

[8]In the 1-D case the useful signal contribution becomes $\boldsymbol{r} = a\left(\boldsymbol{p} + \dot{\boldsymbol{p}}_u \Delta u\right) + \boldsymbol{n}$.

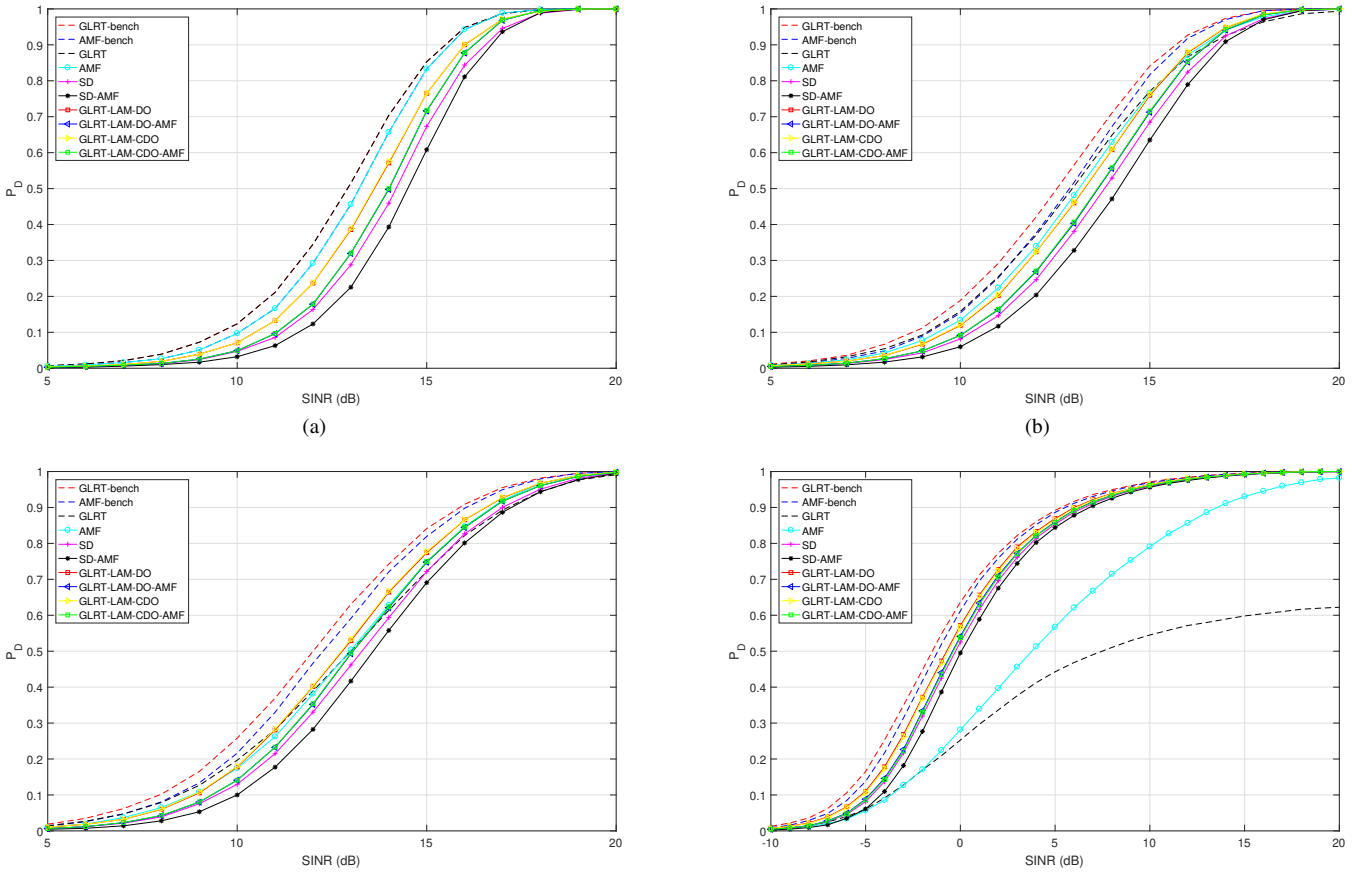

Fig. 5. Detection performance for a URA with 5×5 antennas, $K = 50$ secondary data, and different mismatch conditions, in Scenario 2. The constraint parameters α and β are set at 0.5. The target's location $(\Delta u, \Delta v)$ is modeled as a pair of statistically independent uniform random variables in the region $[-\Delta_1, \Delta_1] \times [-\Delta_2, \Delta_2]$: (a) $(\Delta_1, \Delta_2) = (0, 0)$, (b) $(\Delta_1, \Delta_2) = (0, 0.05)$, (c) $(\Delta_1, \Delta_2) = (0.05, 0.05)$, and (d) $(\Delta_1, \Delta_2) = (0.5, 0.5)$.

To assess the estimation capabilities of the proposed constrained MLE $\widehat{\Delta u}^{\star}$ (see Proposition 1), the MSE versus SINR is displayed in Fig. 4 for different sample support sizes[9], i.e., $K = [16, 32, 48, \infty]$, and target locations, i.e., $\Delta u \in \{0, 0.05, 0.1, 0.5\}$. In this case, $\alpha = 0.2$ and the interfering setup of Scenario 1 is analyzed. Figs. 4(a), 4(b), 4(c), and 4(d) refer to $\Delta u = 0$, $\Delta u = 0.05$, $\Delta u = 0.1$, and $\Delta u = 0.5$, respectively. As expected, the MSE curves decrease with the SINR and the higher K the lower the estimation error (in the mean square sense), being better and better the accuracy of interference covariance matrix estimate.

The results clearly show the effectiveness of the proposed estimator. Indeed, in the high SINR regime, the performance becomes closer to the CRLB benchmark as K increases; of course, this happens when the actual target displacement belongs to the assumed uncertainty region. Otherwise, see Fig. 4(d), the MSE curves reach an error-floor of $(0.5 - 0.2)^2 = -10.4576$ dB. In this last situation, the devised technique reaches the feasible value closest to the actual target displacement, further corroborating the estimation capabilities of the devised strategy. At low SINR, smaller values than the CRLB benchmark are observed indicating that the proposed estimator exhibits a bias under this SINR regime as well as an upper bound to the mean square values induced by the enforced constraint. Indeed, the MSE of the proposed estimator complies with

$$E[(\hat{\theta} - \theta)^2] \leq \max[(\theta - \alpha)^2, (\theta + \alpha)^2], \tag{51}$$

namely, the MSE exhibits a SINR-independent upper bound. On the contrary, equation (77) reported in the supplementary material to this paper shows that the CRLB is unbounded above as the SINR goes to zero. As a result, the performance of our estimator is always better than the CRLB at low SINR. Similar considerations hold true for the MSE behaviour at low SINR, in all the subsequent case studies. Finally, it is also worth noting that the box-and-whisker plots [43] of the two estimation errors reported in Fig. 4(a), reveal the presence of a large number of outliers (points above and below the black whiskers) at low SINR. This behaviour provides a further explanation of the increasing departure of the MSE curves from the CRLB when the SINR ranges in the so called "below threshold region".

Fig. 5 displays P_D curves for the 2-D case, assuming $K = 2MN = 50$, $\alpha = \beta = 0.5$, and Scenario 2. Therein, the displacements vector $(\Delta u, \Delta v)$ is drawn from a uniform distribution over $[-\Delta_1, \Delta_1] \times [-\Delta_2, \Delta_2]$. Specifically, Figs. 5(a), 5(b), 5(c), and 5(d) refer to $(\Delta_1, \Delta_2) = (0, 0)$, $(\Delta_1, \Delta_2) = (0, 0.05)$, $(\Delta_1, \Delta_2) = (0.05, 0.05)$, and

[9] $K = \infty$ is tantamount to considering the exact covariance matrix.

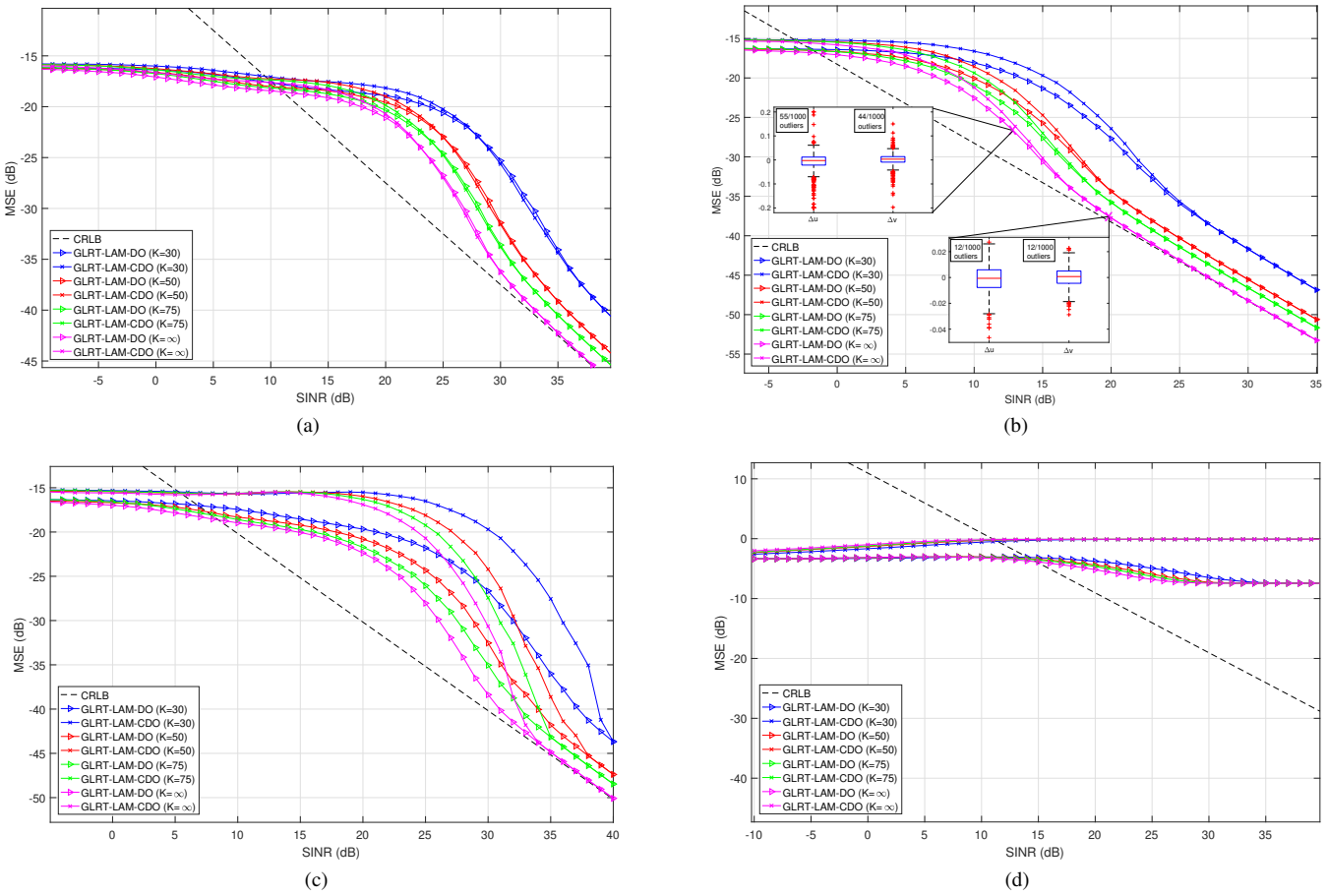

Fig. 6. Estimation performance for a URA with 5×5 antennas in Scenario 2 for different sample support sizes, i.e., $K = [30, 50, 70, \infty]$ and several target locations, i.e., (a) $(\Delta u, \Delta v) = (0, 0)$, (b) $(\Delta u, \Delta v) = (0, 0.05)$, (c) $(\Delta u, \Delta v) = (0.05, 0.05)$, and (d) $(\Delta u, \Delta v) = (0.5, 0.5)$. Therein $\alpha = \beta = 0.2$. In Fig. (b) are also reported two box-and-whisker plots at 13 dB and 20 dB, respectively.

$(\Delta_1, \Delta_2) = (0.5, 0.5)$, respectively. The results show the power of the GLRT-LAM-DO and GLRT-LAM-CDO detector. Indeed, the two algorithms attain the same P_D levels with performance very close to the clairvoyant GLRT-bench, with a loss smaller than 1 dB. Furthermore, apart from the case of $(\Delta_1, \Delta_2) = (0, 0)$, GLRT-LAM-DO and GLRT-LAM-CDO outperform the mismatched detector with performance gains higher and higher as the actual DOA offset region enlarges. Finally, they achieve P_D levels higher than the SD in all the configurations, revealing the capabilities of the new methods to benefit from the underlying structure of the weights. Similar results are achieved by the AMF version of the proposed detectors with respect to their relative counterparts.

Fig. 6 reports the MSE versus SINR for different sample support sizes, i.e., $K = [30; 50; 75; \infty]$, and $\alpha = \beta = 0.2$, with reference to Scenario 2. The target is located at $(\Delta u, \Delta v)$ and Figs. 6(a), 6(b), 6(c), and 6(d) refer to $(\Delta u, \Delta v) = (0, 0)$, $(\Delta u, \Delta v) = (0, 0.05)$, $(\Delta u, \Delta v) = (0.05, 0.05)$, and $(\Delta u, \Delta v) = (0.5, 0.5)$, respectively. As already seen in the 1-D case, the MSE curves decrease with the SINR and the higher K the lower the estimation error (in the mean square sense). In the high SINR regime, the performance approaches the CRLB benchmark as K increases, provided that the actual target displacement lies within the assumed uncertainty region. However, it is also worth pointing out that the MSE lower bound in the scenario of Fig. 6(d) is equal to $(0.5 - 0.2)^2 + (0.5 - 0.2)^2 = -7.4473$ dB and coincides with the error-floor level achieved by the devised techniques. Otherwise stated, in this case at high SINR the feasible point closer to the actual target displacement vector is returned as estimate. Besides, Fig. 6(c) outlines a departure of the MSE curves of GLRT-LAM-CDO and GLRT-LAM-DO. Not surprisingly, they pinpoint the limits of the sub-optimal optimization approach used in GLRT-LAM-CDO with respect to the optimal one used in GLRT-LAM-DO. Finally, the MSE behaviour at low SINR, where smaller values than the CRLB benchmark are achieved, indicates the presence of a bias. As in the 1-D case, the box-and-whisker plots for two operating SINR points, obtained via GLRT-LAM-DO with $K = \infty$ and reported in Fig. 6(b), confirm the role played by the outliers in the departure of the MSE curves from the CRLB.

A computational complexity comparison between GLRT-LAM-DO and GLRT-LAM-CDO is addressed in terms of the average number of iterations involved in the computation of the decision statistics. Assuming as exit condition $\varepsilon_{DO} = 10^{-5}$ and $\varepsilon_{CDO} = 10^{-5}$, the average number of iterations over 100 trials, related to the simulation setup of Fig. 6(b), is given by 20 and 10 for GLRT-LAM-DO and GLRT-LAM-CDO,

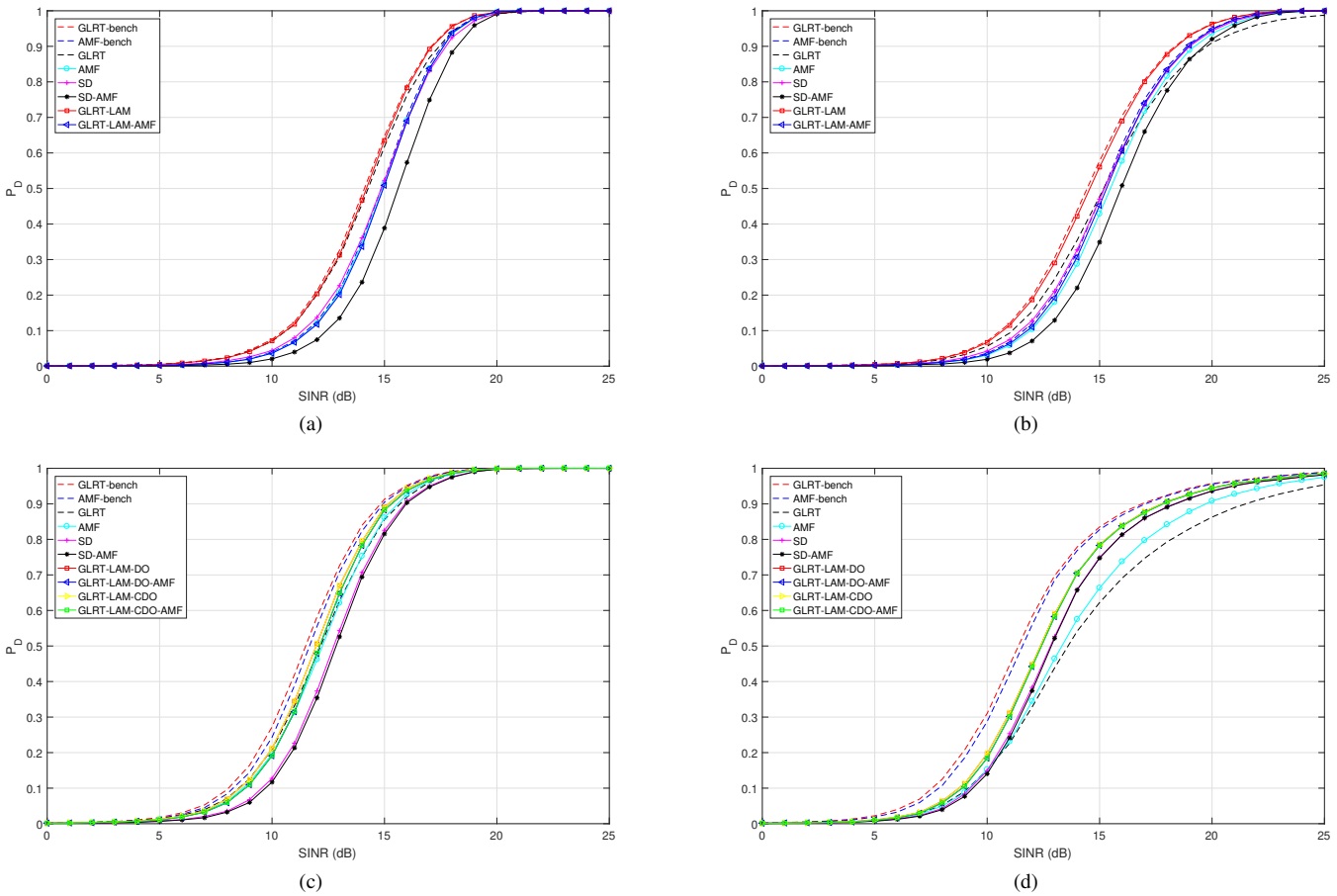

Fig. 7. Detection performance for the actual array manifold assuming the interfering environment of Scenario 3. Figs. (a) and (b) report detection performance for a symmetric ULA with 9 antennas with $K = 18$, target location uniformly distributed over $[-\Delta, \Delta]$, and $\alpha = \Delta$: (a) $\Delta = 0.0523$ and (b) $\Delta = 0.891/N$. Figs. (c) and (d) correspond to a symmetric URA with 5×5 antennas, with $K = 75$, target location offset Δu and Δv modeled as a pair of statistically independent uniformly distributed random variables over $[-\Delta_1, \Delta_1]$ and $[-\Delta_2, \Delta_2]$, respectively, and $\alpha = \Delta_1$, $\beta = \Delta_2$: (c) $\Delta_1 = \Delta_2 = 0.1$ and (d) $\Delta_1 = \Delta_2 = 0.891/5 = 0.1782$.

Methods	Computational Costs
GLRT	$\mathcal{O}(KL^2)$
AMF	$\mathcal{O}(KL^2)$
SD	$\mathcal{O}(KL^2)$
SD-AMF	$\mathcal{O}(KL^2)$
GLRT-LAM	$\mathcal{O}(KN^2)$
GLRT-LAM-AMF	$\mathcal{O}(KN^2)$
GLRT-LAM-DO	$\mathcal{O}(K(NM)^2 + N_{it,b})$
GLRT-LAM-DO-AMF	$\mathcal{O}(K(NM)^2 + N_{it,b})$
GLRT-LAM-CDO	$\mathcal{O}(K(NM)^2 + N_{it,CD})$
GLRT-LAM-CDO-AMF	$\mathcal{O}(K(NM)^2 + N_{it,CD})$

TABLE I
COMPUTATIONAL COMPLEXITY OF THE CONSIDERED PROCESSORS.

respectively. As a consequence, GLRT-LAM-CDO exhibits a reduced computational burden as compared with GLRT-LAM-DO, at the price of a slight performance degradation. Finally, the computational complexity of all the analyzed architectures is provided in Table I, where $L = N$ for the 1-D case whereas $L = NM$, for the 2-D case of the GLRT, AMF, SD, and SD-AMF receivers. Table I emphasizes that the growth curve of the number of operations with respect to the problem size is ruled by the law KL^2.

B. Actual Array Manifold

The considered radar system employs either a ULA of $N = 9$ elements or a URA with 25 elements arranged in a 5×5 square matrix. For both 1-D and 2-D setup, the array points the beam in the boresight direction and the spacing among the elements of the array is $\lambda_0/2$. Moreover, the reference system center coincides with the center of the array. The useful signal contribution is generated according to the actual array manifold, i.e., the steering vector is

$$\boldsymbol{p}(\bar{u} + \Delta u, \bar{v} + \Delta v), \tag{52}$$

with $\bar{u} = \bar{v} = 0$.

For a comparative analysis in terms of angular estimation, the following competitors are considered in the sequel:

- Adaptive Monopulse Estimator, referred to in the following as A-Monopulse and reported in the supplementary material to this paper as Algorithm 4.

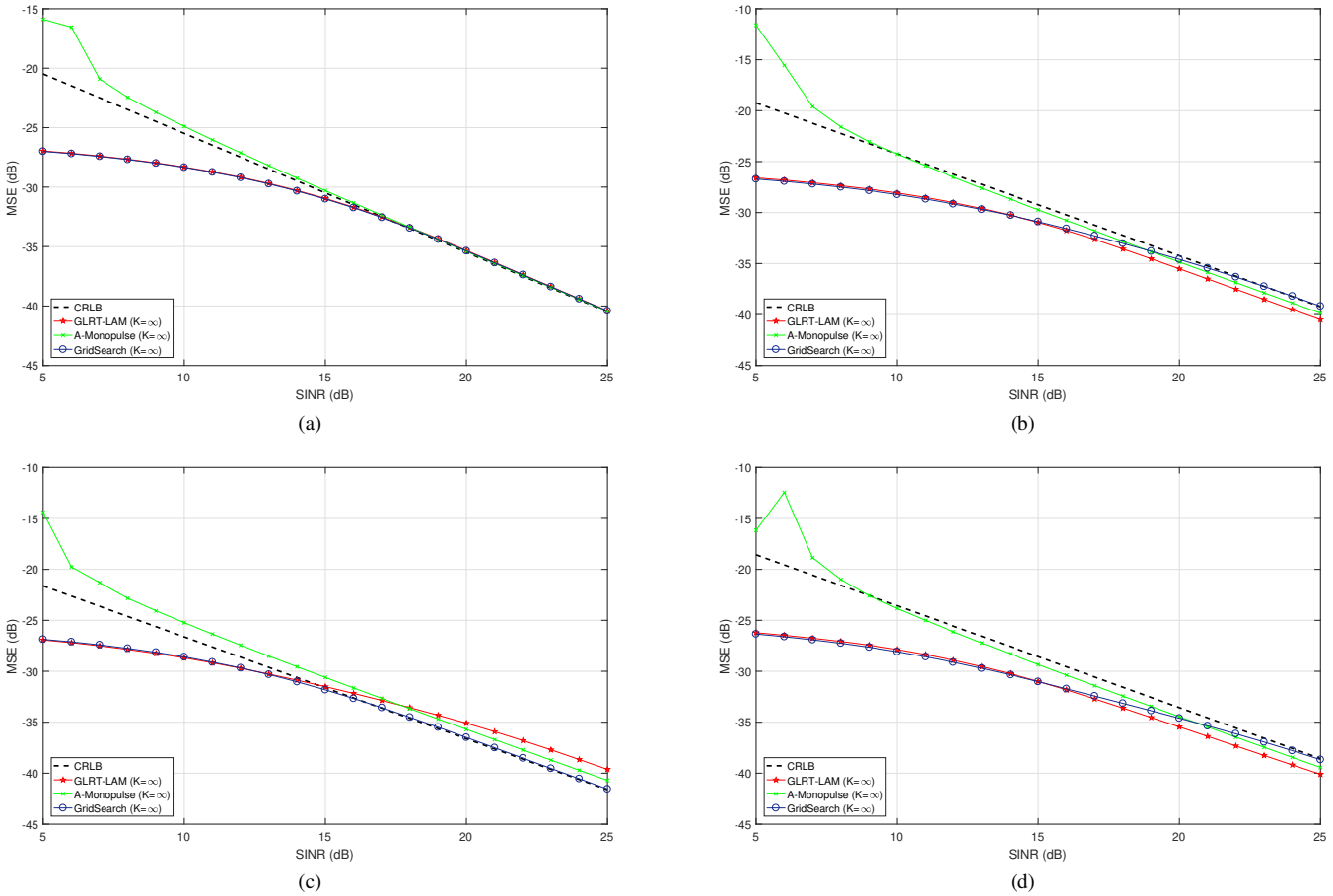

Fig. 8. Estimation performance for a symmetric ULA with 9 antennas in Scenario 3 assuming $K = \infty$ and $\alpha = 0.0523$. The target is located at Δu with (a) $\Delta u = 0$, (b) $\Delta u = 0.01745$, (c) $\Delta u = -0.01745$, and (d) $\Delta u = 0.02618$.

- MLE implementation via grid search (only in the 1-D case), defined as follow

$$\widehat{\Delta u}_{ML} = \underset{\Delta u \in \mathcal{G}}{\arg\max} \frac{\left|\boldsymbol{r}^{\dagger}\boldsymbol{S}^{-1}\boldsymbol{p}(\bar{u}+\Delta u)\right|^2}{\boldsymbol{p}^{\dagger}(\bar{u}+\Delta u)\boldsymbol{S}^{-1}\boldsymbol{p}(\bar{u}+\Delta u)}, \quad (53)$$

where

$$\mathcal{G} = \{-\alpha + i\,\alpha/200, \quad i = 0, \ldots, 400\}. \quad (54)$$

For comparison purposes, the CRLB [10, p. 927, eq. 8.34] is also considered.

Fig. 7 presents detection performance both for the 1-D and 2-D scenarios. The former is considered in Figs. 7(a) and 7(b) under the interfering setup described in Scenario 3 and assuming $K = 18$. The actual DOA displacement is drawn from a uniform distribution over $[-\Delta, \Delta]$, where in Fig. 7(a) $\alpha = \Delta = \sin(3\pi/180) = 0.0523$ while in Fig. 7(b) $\alpha = \Delta = 0.891/9 = 0.099$. The 2-D case is displayed in Figs. 7(c) and 7(d) assuming $K = 75$ and the disturbance environment corresponding to Scenario 3. The target location offsets Δu and Δv are modeled as statistically independent random variable with $\Delta u \sim U(-\Delta_1, \Delta_1)$ and $\Delta v \sim U(-\Delta_2, \Delta_2)$. Fig. 7(c) refers to $\alpha = \beta = \Delta_1 = \Delta_2 = 0.1$ and Fig. 7(d) considers $\alpha = \beta = \Delta_1 = \Delta_2 = 0.891/5 = 0.1782$, respectively. Otherwise stated, in all the figures the design parameters α and β are matched to actual DOA uncertainty.

Inspection of the results shows that the proposed one-step GLRT detectors (GLRT-LAM for the 1-D case, GLRT-LAM-DO and GLRT-LAM-CDO for the 2-D case) ensure a performance level very close to the clairvoyant GLRT and outperform the counterparts for the considered simulation scenarios. Specifically, the P_D curves of the GLRT-LAM and GLRT-LAM-AMF almost overlap with the corresponding benchmark limits. For the 2-D case, GLRT-LAM-DO and GLRT-LAM-CDO experience a slight performance degradation lower than 1 dB at $P_D = 0.9$ with respect to the optimal receiver. Before proceeding further, it is worth pointing out that the proposed joint detection and estimation strategies can be interpreted as two-stage architectures, where first the target direction of arrival is estimated and then a bespoke adaptive detector is applied. For completeness, in the supplementary material the comparison with other two-stage processors (in the sense of performing first the angle estimation with a given technique and then exploiting the resulting estimate within a decision statistic) is reported and discussed.

In Fig. 8 the DOA estimation capabilities of GLRT-LAM, A-Monopulse, and MLE via grid search, are analyzed for the 1-D case, assuming $K = \infty$, $\alpha = 0.0523$, and the interference environment of Scenario 3. Figs. 8(a), 8(b), 8(c), and 8(d) refer to $\Delta u = 0$, $\Delta u = 0.01745$, $\Delta u = -0.01745$, and $\Delta u = 0.02618$, respectively. The exploration of the curves reveals that GLRT-LAM outperforms the A-Monopulse for a wide

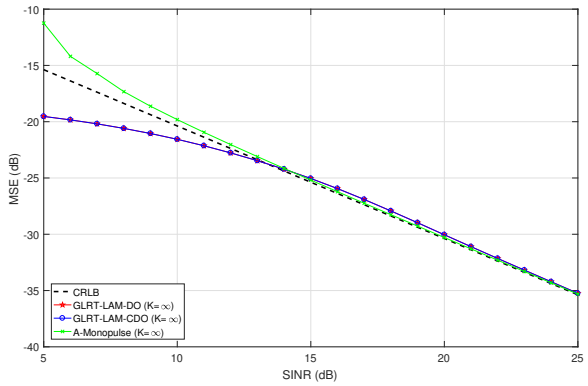

(a)

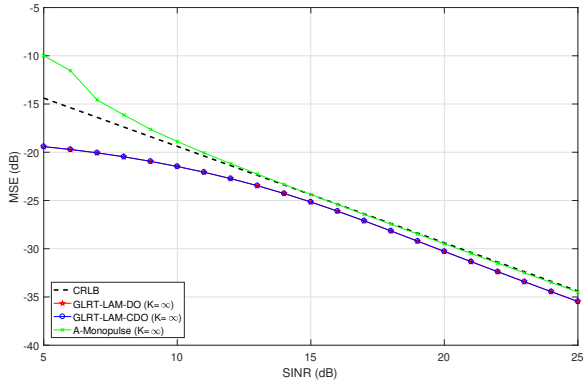

(b)

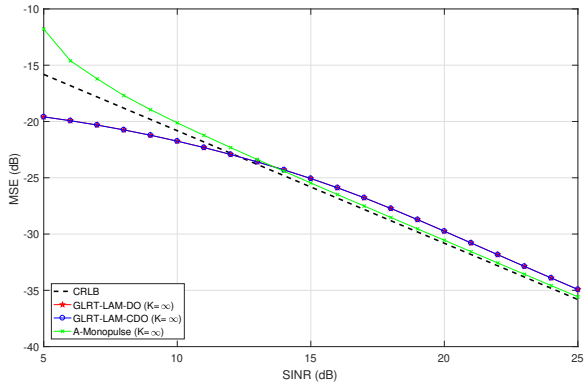

(c)

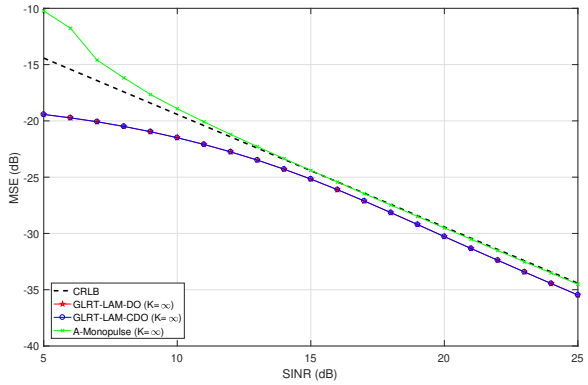

(d)

Fig. 9. Estimation performance for a symmetric URA with 5×5 antennas in Scenario 3 assuming $K = \infty$, $\alpha = 0.1, \beta = 0.1$, and target located at $(\Delta u, \Delta v)$, with (a) $(\Delta u, \Delta v) = (0, 0)$, (b) $(\Delta u, \Delta v) = (0.0349, 0)$, (c) $(\Delta u, \Delta v) = (-0.01745, 0)$, and (d) $(\Delta u, \Delta v) = (0.0349, -0.001218)$.

range of SINR values and provides estimation performance almost overlapped to that of the MLE via grid search method up to a SINR of 20 dB, corroborating the strength of the new devised method. Furthermore, the higher the SINR the lower the MSE of all the estimators regardless of the setup (but for the A-Monopulse in Fig. 8(d) at low SINR) and performance levels comparable with the CRLB benchmark are achieved at the high SINR regime. In this respect, note that possible deviations from the CRLB of the MSE curves (at high SINR) may arise due to the bias of the estimators. Indeed, in the presence of a biased estimator, the general bound to consider is given in [44, p. 147], which can be also lower than the conventional CRLB for unbiased estimators.

Finally, GLRT-LAM and the MLE via grid search achieve MSE values smaller than the CRLB at low SINR, reflecting the presence of a bias in the estimators as well as the limit to the error imposed by the constraint.

The estimation performance for the 2-D case of GLRT-LAM-DO, GLRT-LAM-CDO, and A-Monopulse is analyzed in Fig. 9, considering $K = \infty$, $\alpha = 0.1$, $\beta = 0.1$, where each subfigure refers to a specific target location in the $u - v$ plane. It can be observed that in all the reported case studies GLRT-LAM-DO and GLRT-LAM-CDO achieve the same MSE values and exhibit better estimation capabilities than the A-Monopulse (apart from Fig. 9(b) where a slight loss appears), showing the benefits of the new signal processing strategies. Remarks similar to those made for Fig. 8 hold true with reference to the comparison of the estimators with the CRLB benchmark performance.

Finally, the average number of iterations (over 100 trials) required by GLRT-LAM-DO and GLRT-LAM-CDO in order to converge is 20 and 10, respectively, assuming $\varepsilon_{DO} = \varepsilon_{CDO} = 10^{-5}$ and the simulation setup of 9(b). These results confirm that **Algorithm 3** is usually less demanding than **Algorithm 1**, whilst ensuring satisfactory performance.

To further shed light on **Algorithm 1** estimation performance, Fig. 10 displays the bias and variance ellipses granted by the proposed angle estimator for a grid of 16 displacements between the actual pointing direction and the array steering. The ellipses corresponding to the CRLB are also reported for comparison purposes. The simulation assumes the interference environment of Scenario 3, with $K = \infty$. The results highlight that for (u, v)-displacement in the left bottom corner of the grid (i.e., angle directions far from the jamming DOAs) the variance and CRLB ellipses match quite well. However, when displacements belongs to the upper right corner of the grid, some departures of the variance ellipse from the CRLB are experienced. Besides, as the pointing vector moves towards the jamming DOA, also the bias of the estimator increases.

V. Conclusion

This paper has considered simultaneous detection and target angle localization for a multichannel phased array radar. Signal processing architectures have been proposed which, after target detection, are able to provide directly estimates of the target angular offsets from the array pointing direction. Two estimation procedures respectively based on the Dinkelbach's

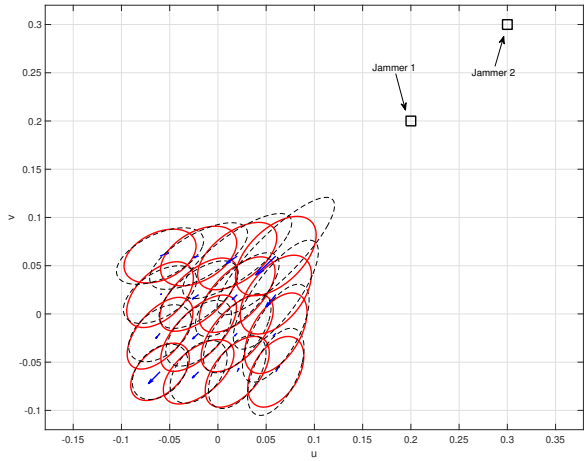

Fig. 10. Bias and variance for a URA with 5×5 elements in Scenario 3 assuming $K = \infty$ and $\alpha = \beta = 0.1$. Dashed black ellipses refer to CRB limit, variances are shown with solid red ellipses whereas the bias vectors are represented by solid blue arrows.

algorithm and a CD method have been devised. The former provides the optimal ML estimates of the unknown displacements. The latter generally exhibits a faster convergence than the former but the optimality of the solution (in the ML sense) cannot be claimed. A comparative analysis has been conducted with other techniques available in the open literature which are either tailored for detection or target angle localization. Benchmark limits have been also considered. The results highlight the interplay of the different design parameters and show that the new algorithms provide adequate performance, thus representing viable solutions for practical implementations.

Possible future research developments might concern the following issues.

1) An analytic study on the bias of the proposed estimation procedure together with the design of techniques (possibly based on multiple iterations) aimed at reducing its effects.
2) The extension of the framework to the polarimetric-spatial domain processing where other degrees of freedom resulting from the use of polarimetric information can possibly boost the performance.
3) The extension of the approach to account for some deviations from the proposed homogeneous disturbance model: i.e., non-Gaussian interference, presence of clutter discretes and/or multiple targets (some possibly fake) within a specific range cell.
4) Design of alternative decision criteria such as the Wald test [32], [45], [46] possibly accounting for rejection of signals outside a specific region in the $u - v$ space [47], [48].

ACKNOWLEDGMENT

The authors would like to thank the Associate Editor for carefully coordinating the revision of this paper and the anonymous Referees for the interesting and pertinent comments.

REFERENCES

[1] M. Rosamilia, A. Aubry, A. De Maio, and S. Marano, "Simultaneous Radar Detection and Constrained Target Angle Estimation via Dinkelbach Algorithm," in *2020 IEEE Radar Conference (RadarConf20)*, Florence, Italy, Sept. 2020.
[2] S. Sabatini and M. Tarantino, *Multifunction Array Radar: System Design and Analysis*, Artech House radar library. Artech House, 1994.
[3] M. A. Richards, W. L. Melvin, J. Scheer, J. A. Scheer, and W. A. Holm, *Principles of Modern Radar: Radar Applications, Volume 3*, Electromagnetics and Radar. Institution of Engineering and Technology, 2013.
[4] M. I. Skolnik, *Radar Handbook, Third Edition*, Electronics electrical engineering. McGraw-Hill Education, 2008.
[5] E. Brookner, "MIMO versus conventional radar performance against jammers," in *2017 IEEE Radar Conference (RadarConf)*, 2017, pp. 0703–0708.
[6] A. Farina, *Antenna-based Signal Processing Techniques for Radar Systems*, Antennas and Propagation Library. Artech House, 1992.
[7] R. Klemm, *Novel Radar Techniques and Applications*, Radar, Sonar and Navigation. Institution of Engineering & Technology, 2018.
[8] U. Nickel, "Overview of generalized monopulse estimation," *IEEE Aerospace and Electronic Systems Magazine*, vol. 21, no. 6, pp. 27–56, 2006.
[9] W. D. Wirth and Institution of Electrical Engineers, *Radar Techniques Using Array Antennas*, Electromagnetics and Radar. Institution of Engineering and Technology, 2001.
[10] H. L. Van Trees, *Optimum Array Processing: Part IV*, Detection, Estimation, and Modulation Theory. Wiley, 2004.
[11] A. S. Paine, "Minimum variance monopulse technique for an adaptive phased array radar," *IEE Proceedings - Radar, Sonar and Navigation*, vol. 145, no. 6, pp. 374–380, 1998.
[12] P. F. Kittredge and N. B. Pulsone, "Wideband angle estimation techniques for a beamspace application," in *Proceedings of the 2000 IEEE Sensor Array and Multichannel Signal Processing Workshop. SAM 2000*, 2000, pp. 474–478.
[13] J. Ward and G. F. Hatke, "An efficient rooting algorithm for simultaneous angle and doppler estimation with space-time adaptive processing radar," in *Conference Record of the Thirty-First Asilomar Conference on Signals, Systems and Computers*, 1997, vol. 2, pp. 1215–1218 vol.2.
[14] A. Farina, G. Gabatel, and R. Sanzullo, "Estimation of target direction by pseudo-monopulse algorithm," *Signal Processing*, vol. 80, no. 2, pp. 295 – 310, 2000.
[15] A. Farina, F. Gini, and M. Greco, "DOA estimation by exploiting the amplitude modulation induced by antenna scanning," *IEEE Transactions on Aerospace and Electronic Systems*, vol. 38, no. 4, pp. 1276–1286, 2002.
[16] A. De Maio, S. De Nicola, A. Farina, and S. Iommelli, "Adaptive detection of a signal with angle uncertainty," *IET Radar, Sonar Navigation*, vol. 4, no. 4, pp. 537–547, 2010.
[17] U. Nickel, "Monopulse estimation with adaptive arrays," *IEE Proceedings F - Radar and Signal Processing*, vol. 140, no. 5, pp. 303–308, Oct 1993.
[18] A. De Maio and M. S. Greco, *Modern Radar Detection Theory*, Electromagnetics and Radar. Institution of Engineering and Technology, 2015.
[19] E. J. Kelly, "An Adaptive Detection Algorithm," *IEEE Transactions on Aerospace and Electronic Systems*, vol. AES-22, no. 2, pp. 115–127, 3 1986.
[20] F. C. Robey, D. R. Fuhrmann, E. J. Kelly, and R. Nitzberg, "A CFAR adaptive matched filter detector," *IEEE Transactions on Aerospace and Electronic Systems*, vol. 28, no. 1, pp. 208–216, 1992.
[21] S. Kraut, L. L. Scharf, and L. T. McWhorter, "Adaptive subspace detectors," *IEEE Transactions on Signal Processing*, vol. 49, no. 1, pp. 1–16, 2001.
[22] O. Besson, "Adaptive detection with bounded steering vectors mismatch angle," *IEEE Transactions on Signal Processing*, vol. 55, no. 4, pp. 1560–1564, 2007.
[23] A. De Maio and D. Orlando, "Adaptive radar detection of a subspace signal embedded in subspace structured plus Gaussian interference via invariance," *IEEE Transactions on Signal Processing*, vol. 64, no. 8, pp. 2156–2167, 2016.
[24] S. Bose and A. O. Steinhardt, "Adaptive array detection of uncertain rank one waveforms," *IEEE Transactions on Signal Processing*, vol. 44, no. 11, pp. 2801–2809, 1996.

[25] D. Ciuonzo, A. De Maio, and D. Orlando, "A unifying framework for adaptive radar detection in homogeneous plus structured interference—part i: On the maximal invariant statistic," *IEEE Transactions on Signal Processing*, vol. 64, no. 11, pp. 2894–2906, 2016.
[26] S. Bose and A. O. Steinhardt, "A maximal invariant framework for adaptive detection with structured and unstructured covariance matrices," *IEEE Transactions on Signal Processing*, vol. 43, no. 9, pp. 2164–2175, 1995.
[27] W. Liu, W. Xie, J. Liu, and Y. Wang, "Adaptive double subspace signal detection in Gaussian background—Part I: Homogeneous environments," *IEEE Transactions on Signal Processing*, vol. 62, no. 9, pp. 2345–2357, 2014.
[28] S. M. Kay, "The multifamily likelihood ratio test for multiple signal model detection," *IEEE Signal Processing Letters*, vol. 12, no. 5, pp. 369–371, 2005.
[29] D. Orlando and G. Ricci, "Adaptive radar detection and localization of a point-like target," *IEEE Transactions on Signal Processing*, vol. 59, no. 9, pp. 4086–4096, 2011.
[30] M. Xing, J. Su, G. Wang, and Z. Bao, "New parameter estimation and detection algorithm for high speed small target," *IEEE Transactions on Aerospace and Electronic Systems*, vol. 47, no. 1, pp. 214–224, 2011.
[31] W. Yi, T. Zhou, Y. Ai, and R. S. Blum, "Suboptimal low complexity joint multi-target detection and localization for non-coherent mimo radar with widely separated antennas," *IEEE Transactions on Signal Processing*, vol. 68, pp. 901–916, 2020.
[32] S. M. Kay, *Fundamentals of Statistical Signal Processing: Detection theory*, Prentice Hall Signal Processing Series. Prentice-Hall PTR, 1998.
[33] S. Siegfried, "Fractional Programming - 2. on Dinkelbach'S Algorithm.," *Management Science*, vol. 22, no. 8, pp. 868–873, 4 1976.
[34] J. P. Crouzeix and J. A. Ferland, "Algorithms for generalized fractional programming," *Math. Program.*, vol. 52, no. 1–3, pp. 191–207, May 1991.
[35] A. I. Barros, J. B. Frenk, S. Schaible, and S. Zhang, "A new algorithm for generalized fractional programs," *Math. Program.*, vol. 72, no. 2, pp. 147–175, Feb. 1996.
[36] B. Chen, S. He, Z. Li, and S. Zhang, "Maximum block improvement and polynomial optimization," *SIAM J. on Optimization*, vol. 22, no. 1, pp. 87–107, Jan. 2012.
[37] R. S. Raghavan, N. Pulsone, and D. J. McLaughlin, "Performance of the GLRT for adaptive vector subspace detection," *IEEE Transactions on Aerospace and Electronic Systems*, vol. 32, no. 4, pp. 1473–1487, 1996.
[38] F. Bandiera, O. Besson, and G. Ricci, "An abort-like detector with improved mismatched signals rejection capabilities," *IEEE Transactions on Signal Processing*, vol. 56, no. 1, pp. 14–25, 2008.
[39] M. Steiner and K. Gerlach, "Fast converging adaptive processor or a structured covariance matrix," *IEEE Transactions on Aerospace and Electronic Systems*, vol. 36, no. 4, pp. 1115–1126, 2000.
[40] M. A. Lodhi and W. U. Bajwa, "Detection theory for union of subspaces," *IEEE Transactions on Signal Processing*, vol. 66, no. 24, pp. 6347–6362, 2018.
[41] R. L. Berger and D. F. Sinclair, "Testing hypotheses concerning unions of linear subspaces," *Journal of the American Statistical Association*, vol. 79, no. 385, pp. 158–163, 1984.
[42] D. P. Bertsekas, *Nonlinear programming*, Athena Scientific, Belmont, Massachusetts, 1999.
[43] J. W. Tukey, *Exploratory Data Analysis*, Exploratory Data Analysis. Addison Wesley Publishing Company, 1970.
[44] H. L. Van Trees, *Detection, Estimation, and Linear Modulation Theory: Part I*, Detection, Estimation, and Modulation Theory. Wiley, 2001.
[45] A. Wald, "Tests of statistical hypotheses concerning several parameters when the number of observations is large," *Transactions of the American Mathematical Society*, vol. 54, no. 3, pp. 426–426, Mar. 1943.
[46] A. J. Lemonte and S. L. P. Ferrari, "The local power of the gradient test," *Annals of the Institute of Statistical Mathematics*, vol. 64, no. 2, pp. 373–381, Oct. 2010.
[47] N. B. Pulsone and C. M. Rader, "Adaptive beamformer orthogonal rejection test," *IEEE Transactions on Signal Processing*, vol. 49, no. 3, pp. 521–529, 2001.
[48] F. Bandiera, A. De Maio, and G. Ricci, "Adaptive CFAR radar detection with conic rejection," *IEEE Transactions on Signal Processing*, vol. 55, no. 6, pp. 2533–2541, 2007.